# An Evaluation of Patient-Specific IMRT Verification Failures

by

**Jason Crawford**
BSc, University of British Columbia, 2007

A Thesis Submitted in Partial Fulfillment of the
Requirements for the Degree of

**Masters of Science**

in the Department of Physics and Astronomy



University of Victoria

**An Evaluation of Patient-Specific IMRT Verification Failures**

by

**Jason Crawford**

BSc, University of British Columbia, 2007

# Supervisory Committee

---

Dr. I. M. Gagne, Co-supervisor

British Columbia Cancer Agency - Vancouver Island Centre

& Department of Physics and Astronomy

---

Dr. A. Jirasek, Co-supervisor

Department of Physics and Astronomy

---

Dr. W. Ansbacher, Member

British Columbia Cancer Agency - Vancouver Island Centre

& Department of Physics and Astronomy

# Supervisory Committee

---

Dr. I. M. Gagne, Co-supervisor

British Columbia Cancer Agency - Vancouver Island Centre

& Department of Physics and Astronomy

---

Dr. A. Jirasek, Co-supervisor

Department of Physics and Astronomy

---

Dr. W. Ansbacher, Member

British Columbia Cancer Agency - Vancouver Island Centre

& Department of Physics and Astronomy

## Abstract

At the BC Cancer Agency (BCCA), Vancouver Island Centre (VIC), the clinical verification of Intensity Modulated Radiation Therapy (IMRT) treatment plans involves comparing Portal Image (PI) -based three-dimensionally reconstructed (EPIDose) dose distributions to planned doses calculated using the Pencil Beam Convolution (PBC) algorithm. Discrepancies surpassing established action levels constitute failure. Since 2007, the failure rate of IMRT verification process had been increasing, reaching as high as 18.5% in 2009. A retrospective evaluation of clinical IMRT verification failures was conducted to identify causes and possible resolutions. Thirty clinical verification failures were identified. An equipment malfunction was discovered and subsequently repaired, and several failures were resolved in the process.

Statistical uncertainty in measurement outcome was small in comparison to action levels and not considered significant to the production of failures. Still, over 50% of the redelivered plans were shown to consistently fail. A subgroup of consistent verification plans were compared to ion chamber point dose measurements. Relative to ion chamber measurements, EPIDose underestimated the dose while the dose calculation algorithm (PBC, Eclipse version 8.1.18) overestimated the same point dose. Comparisons of individual fields demonstrated that none were identifiably problematic; dose discrepancies were the result of minor but accumulating dose differences. Consistent verification failures were recalculated using two advanced dose calculation engines (the Anisotropic Analytical Algorithm and Monte Carlo). In general, verification metrics improved, and all failures were resolved. Three distinct indices of fluence modulation (or complexity) were shown to correlate with verification metrics. This indicated that deficiencies in both the leaf motion calculator and the PBC (Eclipse version 8.1.18) had likely contributed to the production of failures. In conclusion, clinical verification failures were resolved retrospectively by replacing faulty equipment and using more advanced methods of planned dose calculation, supporting the efficacy and continued use of PI-based three dimensional dose reconstruction for IMRT verification.

# Table of Contents

# List of Tables

# List of Figures

## Acknowledgements

I would like to express sincere gratitude to my co-supervisors, Isabelle Gagne and Andrew Jirasek, and committee member, Will Ansbacher, for providing me so generously with education, direction, confidence and understanding during my time as their student. I would like to extend this appreciation to the entire Physics department at VIC for continually maintaining an inspiring, positive, and cohesive workplace. I am truly privileged to be a part of this group. Special thanks to Karl Bush for countless contributions, not only in technical expertise, but also for invaluable guidance throughout my graduate experience. My success would not have been possible without the incredible support I received from my brother, Joe Crawford, and the rest of my amazing and loving family. Thank you all.

# Chapter 1

# Introduction

Cancer is the leading cause of death in Canada. [1]. An estimated 173,800 Canadians will be diagnosed with cancer in 2010 (171,000 in 2009)[1], and approximately one in four Canadians will die from cancer [1]. Moreover, the incidence of cancer is increasing with the growing and aging Canadian population [1]. Effective cancer care and management strategies rely on the quality and safety of the prescribed treatment.

The treatment of cancer requires eliminating masses of cancer cells (or *malignant neoplasms*), through mitotic death or apoptosis [2]. A mass of cells experiencing uncontrolled (or unregulated) cell growth and division is referred to as a *tumour*, and is sometimes cancerous when invasive to surrounding healthy normal tissue [2]. This is the result of abnormalities (or mutations) in genetic information encoded in the damaged DNA of susceptible cells [2]. Malignant (cancerous) tumours are capable of invading nearby healthy tissue and moving to and damaging any part of the body[2] [2]. In particular, cancer cells detach and move from the primary tumour through the blood stream or lymphatic system, producing additional cancerous tumours, called metastases [2]. The invasive and destructive properties of malignant tumours cause life-threatening physiological complications.

The field of medicine associated with cancer is referred to as *Oncology*. This dis-

[1]Numbers of incidence exclude 75,500 non-melanoma skin cancers.

[2]Benign (non-cancerous) tumours are noninvasive and localized in the body.

cipline includes over 100 diseases, most of which are characterized by the presence of malignant tumours. Cancer management is primarily pursued in three ways: surgery, chemotherapy, and radiation therapy. Less but increasingly-common strategies include immunotherapy and the complementary therapies of alternative medicine. These modalities are often combined to provide the best available curative or palliative cancer management strategy [2]. More than half of cancer patients receive radiation therapy [2].

## 1.1 Radiation therapy

Ionizing radiation is capable of causing irreparable damage to DNA and thus can be used to inhibit the function and replication of tumour cells [2, 3]. The objective of radiation therapy is to deliver a prescribed amount of ionizing radiation (or *dose*) to the tumour while limiting the complications of dose to surrounding normal tissues. While the prescribed doses of radiation are designed to cause tumour regression (and eventual local control), they must also minimize the inevitable consequences of subjecting healthy tissue to radiation. Cancer cells are more susceptible to radiation than most normal human cells, due in part to the higher rate of tumour cell replication and the irregular structure of cancer cell DNA [2, 3]. Still, damaging healthy tissue can inhibit proper physiological functions and lead to a reduction in the patient's quality of life. Although different organs vary in their physiological response to radiation, organ-specific dose tolerances have been established from reviewing patient outcomes and the collective knowledge of several experienced oncologists [4].

Ionizing radiation can damage DNA by either breaking the DNA molecule directly or via the production of highly-reactive (and consequently destructive) free radicals in the vicinity of DNA [2, 3]. The extent of damage is a direct result of the amount of energy deposited per unit mass, called the *absorbed dose*. The most prevalent form of radiation used in the treatment of cancer are photons at energies ($E_\gamma$) on the order

of $10^{-1}$ MeV to $10^{1}$ MeV[3] [5]. Photon interactions with tissue (and matter, in general) are well understood, and include: coherent scattering, the photoelectric effect, Compton Scattering, and pair production ($E_\gamma > 1.022$ Mev) [8]. The probability of any one type of photon interaction is definite and related to $E_\gamma$ and the properties of the medium. For this reason, the intensity of a monoenergetic photon beam with zero divergence exhibits exponential attenuation with distance traversing a medium, as, for a given distance, an equal fraction of the incident number of photons is removed. With the exclusion of coherent scattering, these interactions produce highly-energetic *secondary* electrons that dissipate energy as they are slowed down by ionization interactions with the medium[4]. By overlapping the collimated radiation from multiple source positions, a therapeutic dose can be localized at an arbitrary depth inside the patient. This provides a noninvasive means of selectively destroying cancer cells surrounded by healthy tissue, with direct curative or palliative benefits to the patient.

Radiation can be delivered to the tumour from a source positioned at a distance from the body, a technique called *external beam radiation therapy* [5]. Another technique, *brachytherapy*, involves positioning radiation-emitting isotope sources within or in close proximity to the body [5]. The choice in treatment strategy is specific to the type (or site) and stage of disease as well as any additional conditions relating to the particular circumstances of the patient.

The planning of curative external beam radiation therapy typically begins with a Computed Tomography (CT) scan of the patient for a fixed setup that can be replicated at the time of treatment delivery. The 3-dimensional anatomical information is then imported into a computerized Treatment Planning System TPS that is used to manage and optimize the treatment. In this way, the Planning Target Volume

[3]Alternatives to primary photon radiation include –but are not limited to– electrons, protons and heavy ions [5–7].

[4]In the event of pair production, the emitted positron will also dissipate energy before it is annihilated.

(PTV)[5], each Organ-At-Risk (OAR), and relevant patient anatomy are described in a 3-dimensional virtual environment.

Multiple fields of radiation (or *beams*) are positioned with respect to the patients anatomy, simulating the conditions of the treatment, and configured in a way such that the resulting dose distribution meets the requirements of the prescription. Multiple collimated radiation fields from different beam directions are overlapped at the target's location, attempting to produce dose distributions that are conformal and uniform to the target volume, while reducing the dose distributed to healthy tissue. Satisfactory dose distributions can be achieved by calculating dose distributions iteratively while manipulating beam parameters (forward planning), or by implementing an optimization algorithm based on predefined dose-volume constraints (inverse planning) [9]. Once a suitable plan has been determined, patients are positioned appropriately at the treatment unit and the planned radiation fields are delivered.

Several modalities of external beam radiation therapy exist. Three-dimensional Conformal Radiation Therapy (3D-CRT) employs multiple beams of uniformly distributed radiation intensity that are peripherally collimated to match PTV geometry [9]. Given the limited degrees of freedom in the parameters of this strategy, some instances unavoidably result in unacceptable dose to OARs in close proximity to the PTV. Better conformity can be achieved by allowing the radiation intensity profile of each field to vary spatially, a technique called Intensity Modulated Radiation Therapy (IMRT) [10].

Other treatment options include several methods where the source of radiation is rotated around the patient during treatment, spreading out the non-target dose to a larger volume of healthy tissue. Ultimately, all treatment modalities have a unique set of advantages and disadvantages and the proper implementation of the most modern techniques is an active area of research [11].

[5]The PTV is a volume including the tumour, as well as a margin to account for microscopic disease, movement, and uncertainty in delivery.

## 1.2 The principles of IMRT

Although IMRT is a considerably new and advanced technique in radiation therapy, favourable clinical success and large-scale investments have contributed to widespread implementation [12]. IMRT provides therapeutic benefits for several sites of disease, including cancers of the head and neck (H&N), breast, prostate, spine, brain, and many others. At the BC Cancer Agency (BCCA) Vancouver Island Centre (VIC) IMRT is primarily used for the treatment of H&N cancer. Additional uses include some breast and brain treatments.

IMRT fields can be described as arrays of independently intensity-weighted beam-elements [13]. Excessive dose to critical structures is avoided by reducing the intensity of parts of the beam intersecting the OAR, while the reduction in dose to the PTV is compensated for by complementary portions of other fields. The high number of variable parameters involved in an IMRT plan require computerized optimization routines to compute the best achievable IMRT fluences. In these methods, the relationship and relative importance of PTV and OAR dose-volume objectives are described mathematically in the form of a *cost function*, which is then subjected to a minimization algorithm [13].

Several techniques for creating the necessary modulation of IMRT fluences are available [10]. Currently, the most common (conventional) method of delivery is *sliding window* (or *dynamic*) IMRT (dMLC IMRT). In dynamic IMRT, the desired beam-space intensity variations are produced by coordinating the movement of geometrically-dynamic beam-collimating apertures across the field during delivery. This method requires an array of independently-controlled, highly-attenuating, narrow metal plates (or *leaves*) capable of extending (and retracting) arbitrary distances into (and out of) the beam, collectively referred to as the Multileaf-Collimator (MLC).

## 1.3 The verification of IMRT

Every IMRT treatment involves a highly-complicated delivery with many components and assumptions, and is for these reasons susceptible to error. The safe and effective delivery of IMRT depends on following a well-defined Quality Assurance (QA) program [14]. General aspects of delivery can be evaluated at regular time intervals, such as patient positioning accuracy or the proper functioning of equipment [9]. Moreover, IMRT requires a *patient-specific* QA program whereby the quality of clinical planning and delivery is addressed for each treatment on an individual basis[14]. Patient-specific QA should precede the first day of treatment, by which time all significant problems related to the treatment should be resolved. Planned (calculated) doses can be verified with independent calculations and by measuring the delivered dose.

LoSasso *et al* demonstrated that minor 1 mm errors in MLC-leaf positioning for 1 cm-wide sliding window dMLC fields can translate to dose discrepancies as high as ten percent [15]. Minor changes in collimator, gantry, and couch angle have been shown to produce significant inaccuracies in dose delivery [15]. Verification measurements are meant to address the inevitable errors associated with IMRT delivery, and evaluate the dosimetric significance. Verification is also a means of validating (or negating) the assumptions made by the TPS in calculating the planned dose distribution. In addition, the process also verifies that data is transferred successfully from the TPS to the treatment unit, and that the treatment can be delivered as planned.

Depending on the method of measurement, verification analysis can be made by evaluating either the differences between planned (calculated) and delivered (measured) dose distributions or by comparing expected and delivered fluences directly [9]. At VIC, IMRT fluences are evaluated qualitatively while dose discrepancies are quantified in terms of specific metrics which can be compared to predefined toler-

ance criteria, known as *action levels*. Properly chosen action levels indicate whether or not the dose discrepancy is considered significant to the treatment. In addition, these comparisons can be used to alert the department to statistically unexpected occurrences in the IMRT process [16]. When the discrepancies between the planned and measured dose distributions are found to surpass a given action level, the plan is identified as a failure. Failures are typically confirmed by one or more repeated measurements.

In general, there are three distinct reasons for IMRT verification failure. First, delivery errors may occur, possibly related to the physically-demanding delivery of IMRT. Second, accuracy of the measurement technique may be compromised for some unforeseen reason. Third, the approximations made by the TPS dose calculation algorithm may be inadequate. In the event of IMRT verification failure at VIC, the treatment is either replanned, or delivered following consultation and review with the radiation oncologist.

## 1.4 Overview of clinical IMRT verification at VIC

In December of 2005, VIC implemented a novel technique for measurement-based IMRT verifications, a process called portal image-based 3-dimensional dose reconstruction [17]. Figure 1.1 presents a corresponding timeline related to the VIC IMRT verification process. During the period of 2007 and 2008, anterior neck sparing was gradually introduced as an additional planning objective of H&N IMRT. This required that a mid-line critical structure (including the esophagus, trachea, and larynx) be avoided, and thus be considered by the fluence optimization process. The result has been an increase in the the average modulation of H&N IMRT fields at VIC. An example of the change in fluence arising from mid-line neck sparing is shown in Figure 1.2. In theory, the effective planning and delivery of IMRT plans with mid-line neck sparing is relatively more difficult. Speculatively, a relationship was considered

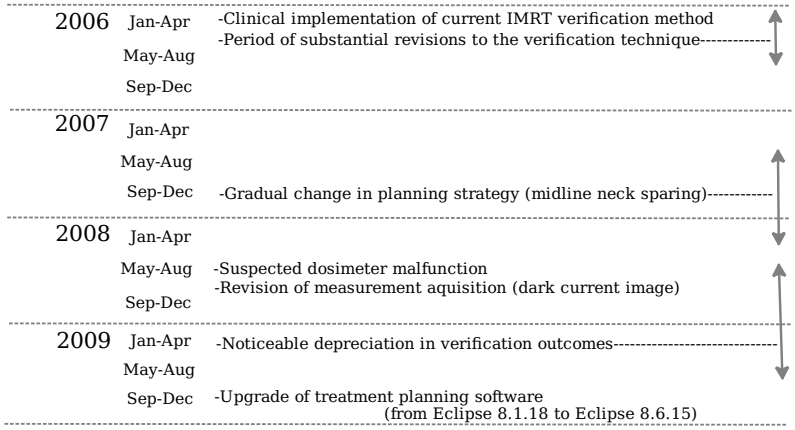


**Figure 1.1:** A timeline of events and observations at VIC related to IMRT verification Jan 2006 - Oct 2009).

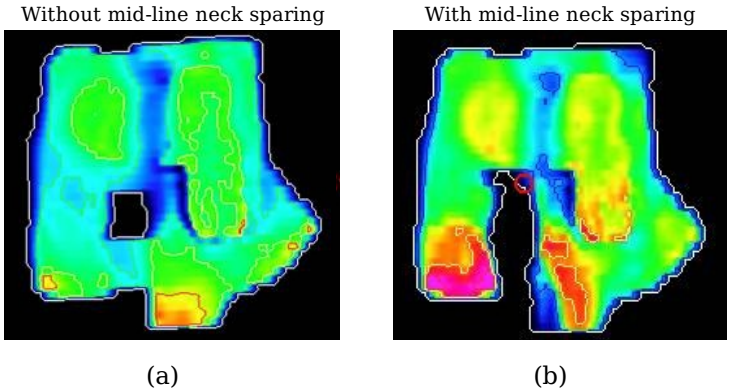


**Figure 1.2:** An IMRT field optimized **(a)** without mid-line neck sparing, and **(b)** with mid-line neck sparing. Midline neck sparing translates to considerably more modulation.

to exist between the fluence modulation and verification outcome of a plan. Evaluation of this potential relationship was confounded by additional circumstances. Deficiencies in the measurement equipment were suspected in the summer of 2008. This led to considerable revision of the processing of verification measurements. Following these revisions, verification outcomes continued to worsen, without an obvious means of resolution. In October of 2009, a software upgrade was made to the TPS.

Between January of 2006 and October of 2009 (inclusive), VIC treated over 300 IMRT patients. Since 2007, there has been an annual increase in the percentage of verification failures (where one or more action level has been exceeded in each case), becoming higher than 18 percent. The trend in failure rate is shown in Figure 1.3.

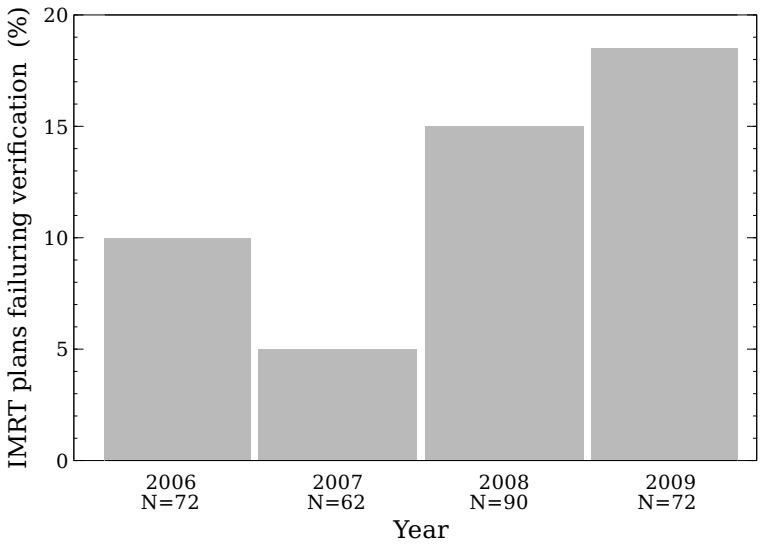


**Figure 1.3:** The annual percentage of IMRT plans that failed verification, for the years 2006-2009. These findings exclude a small number of rarely-treated sites.

Each verification failure represents an increased investment in time, either in re-execution of verification, or replanning. In addition, verification failures signified the possibility of deficiencies in the process, with possible implications to the quality of patient care. It was unclear to what end this trend in failure would continue, and thus, the reasons for the rising failure rate required an extensive evaluation.

## 1.5 Thesis scope

As described above, errors in delivery, measurement and calculation had potentially contributed to the production of verification failures. It was necessary to retrospectively investigate the verification process and identify components of the IMRT process that were most significant to the production of failures. Specifically, this involved the independent analysis of three distinct aspects of IMRT verification outcomes. The first was evaluating the consistency of verification outcomes and addressing any irregularities of the measurement process, directly establishing the significance of the joint statistical uncertainty in delivery and measurement. Second, the relative importance of errors in planning calculation and verification dosimetry were also investigated. This involved a series of independent measurements and calculations. Ion chamber measurements were used to provide trusted, reliable point dose measurements to serve as a reference, while dose distributions were volumetrically compared to the results of advanced, more-accurate means of dose calculation. Third, the impact of fluence complexity was evaluated. This analysis involved correlating quantitative indices of fluence modulation to the outcome of verification metrics. By identifying systematic similarities among verification failures, the most critical mechanisms of verification failure were discovered and provided a basis for reducing failure rate in the future.

# Chapter 2

# Background

## 2.1 The delivery of IMRT

### 2.1.1 The modern linear accelerator

The dose distributions of IMRT are delivered with a therapeutic linear accelerator (linac). This device is a common and central part of external beam radiotherapy. The linac produces a polyenergetic beam (or fluence) of photons originating from a finite source. The photon fluence is measured, collimated and modulated to the specifications of the IMRT plan before exiting the linac *treatment head*. The linac treatment head is mounted on a gantry which is capable of revolving 360° around a single point, called the *isocentre*. This allows for the delivery of successive IMRT fluences from different gantry angles (GA) for a fixed patient setup.

The X-ray beam is produced by high energy electrons colliding inelastically with a metal target, usually tungsten (W). When electrons experience the coulomb force presented by a heavy nucleus, part of their energy is emitted as an X-ray (known as *bremsstrahlung*) [8], as shown in Figure 2.1a. All or some of the incident electron energy may be transferred to the bremsstrahlung photon, producing a continuous spectrum of photon energies [8]. The remaining energy of the electron beam is mostly deposited in the target as heat. An example of a 6 MV photon linac energy spectrum

(a result of 6 MeV electrons incident on a W target) is shown in Figure 2.1b. Lower energy Bremsstrahlung are preferentially attenuated by the target, being removed from the spectrum.

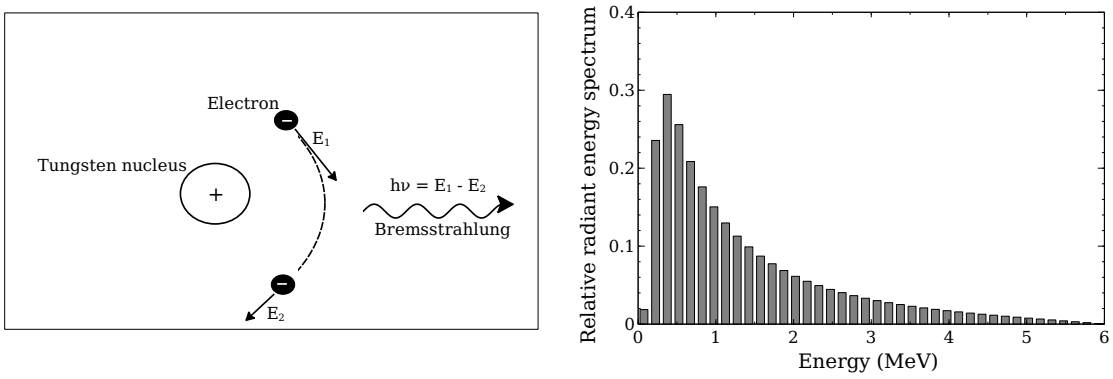


(a) (b)

**Figure 2.1: (a)** An illustration of the bremsstrahlung produced when an electron collides with a tungsten target, and **(b)** an example of the resulting photon energy spectrum for 6 MeV electrons incident on the tungsten target of a linac (data courtesy of K. Bush, 2010 unpublished). Up to 100% of the incident electron energy may be transferred to the bremsstrahlung, and the energy spectrum is continuous. Low energy photons are mostly attenuated by the target, and removed from the spectrum.

At VIC, the Varian Clinac 21EX (Varian Medical Systems, Palo Alto, CA, USA) is used for all IMRT deliveries. Principle components of the Varian Clinac 21EX treatment head are shown schematically in Figure 2.2. Bremsstrahlung originating at the target have a forward-biased angular intensity distribution and diverge from the source [8]. The *primary collimator* is fixed immediately after the target and removes photons traveling outside a defined divergence from the central beam axis [9]. The forward-biased photon intensity distribution is made uniform using a flattening filter, which is an attenuating cone centered on the central (beam) axis [9]. Ion chambers are used to measure beam uniformity and intensity, and provide a relative measure of radiation output, counted in *Monitor Units* (MU) [9].

A treatment-specific field size is defined by two pairs of beam blocks that move in orthogonal directions, called the *secondary collimator* [9]. Each beam block (or *jaw*) can be moved with respect to the central beam axis to create a rectangular field with

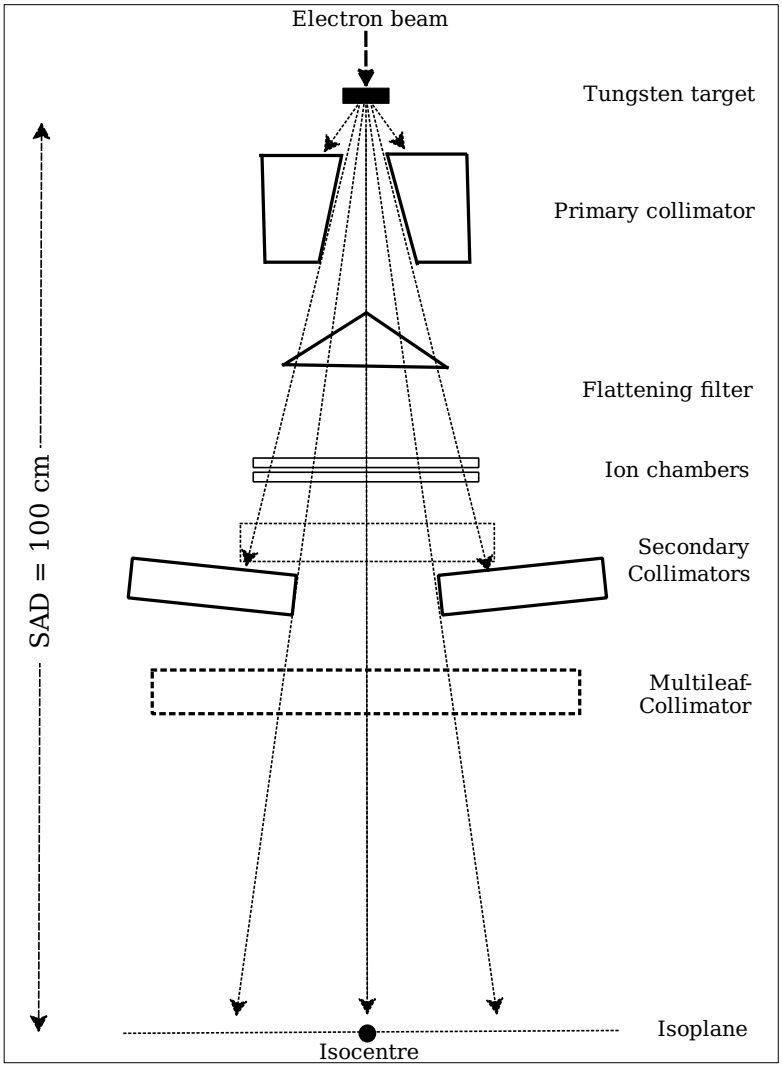


**Figure 2.2:** Configuration of linac treatment head components.

sizes ranging up to 40x40 $cm^2$ at the isoplane[1]. The two pairs of jaws are referred to as X and Y, with the position of each jaw (X1, X2, Y1, Y2) denoting the field edge it defines at the isoplane. The entire secondary collimator and thus the shape of the exiting fluence can be rotated about the beam axis by 360°, the *collimator angle* (Col.A). The fluence intensity distributions required for IMRT are created using a tertiary collimator, called the *Multileaf-Collimator*.

### 2.1.2 The multileaf-collimator

Distal to the secondary collimator of the Varian Clinac 21EX is the Multileaf-Collimator (MLC). The MLC is used to collimate the beam to match the profile of the target, as well as modulate the intensity of IMRT fields. The MLC is composed of 120 tungsten alloy *leaves* that can be extended or retracted to produce a desired (plan-specific) collimated aperture [9]. The apertures can be made to change dynamically throughout delivery (dose mode) to produce the desired intensity modulation, a delivery method known as dynamic MLC (dMLC) IMRT [9]. Alternatively, several IMRT fields can be combined to produce the intended intensity modulation (static mode), sometimes referred to as step-and-shoot IMRT. At VIC, IMRT is mostly delivered with dMLC. One exception includes few-segment IMRT (fsIMRT), for which the desired intensity modulations are achieved with a small number of static fields, manually selected by an experienced dosimetrist.

Each MLC leaf is 6.5 cm thick (parallel to the beam axis), 19 cm long (in the direction of movement), and independently operated by a unique motor that is capable of one dimensional extension/retraction on a plane perpendicular to the beam axis [9]. The MLC leaves are divided into two equal groups (each connected to one of two *carriages*) on either side of the beam axis, and oriented so that leaves are paired and rest facing each other. Each carriage group consists of 40 central leaves of 0.5

[1]The isoplane is a plane in space perpendicular to the central beam axis and for which the isocentre is a point.

cm width and 20 outer leaves (10 on each side of the central group) 1 cm wide, as projected to isocentre [9]. An individual leaf has one side with a rectangular projection (called a tongue) complemented by a rectangular cavity (called a groove) on the other side [9, 15]. In this way, adjacent leaves are fit together in a tongue-and-groove design (Figure 2.3a), significantly reducing inter-leaf radiation leakage [18]. Leaf-tips are rounded to account for the otherwise off-axis dosimetric differences at the field edge (or *penumbra*, caused by the planar orientation of the MLC with respect to a diverging beam (Figure 2.3b) [9, 15].

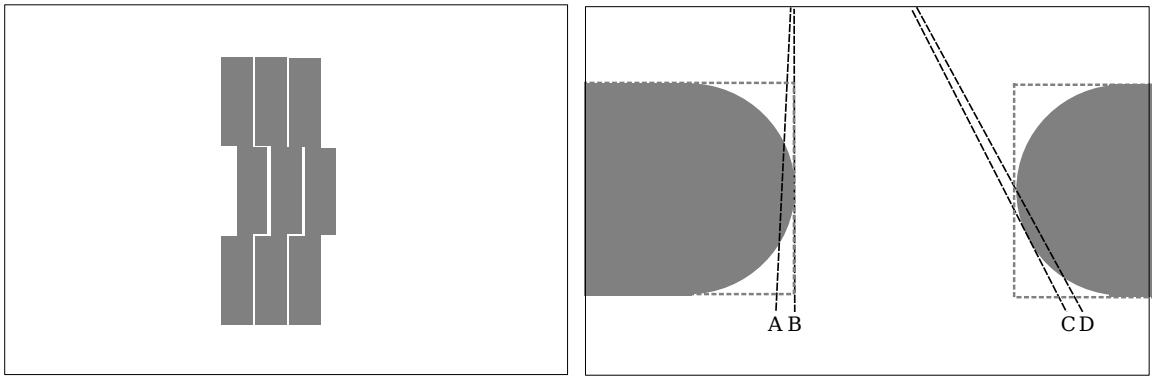


**Figure 2.3:** **(a)** MLC tongue-and-groove design, and **(b)** rounded MLC leaf-tips. As depicted, rounded leaf tips provide a dosimetric convenience: pairs of fan-lines (A and B, C and D) with equal divergence are attenuated by the same difference in thickness of tungsten. This corresponds to fairly similar penumbra (compared to flat leaf-tips). In this example, the curvature of the leaf tips has been exaggerated and in reality the radius is 12 cm.

## 2.2 Calculation of IMRT dose distributions

The inverse planning of an IMRT dose distribution produces an *optimal fluence* for each field. A Leaf Motion Calculator (LMC) is then used to determine a dMLC leaf sequence that approximates the optimal fluence [19, 20]. The deliverable fluences, determined by physical motion of the MLC leaves, can then be approximated by an *actual fluence*. Calculation of the actual fluences involves accounting for MLC transmission and rounded MLC leaf-tips. Approximation of MLC transmission does

not consider inter-leaf and intra-leaf transmission separately, and instead is given by a single averaged transmission factor. The rounded MLC leaf tips are not explicitly modeled, but instead are approximated by an offset value to leaf position, called the Dosimetric Leaf Separation (DLS). MLC transmission and DLS are chosen to optimize agreement between measurement and calculation. These parameters have been shown to be dependent on field size and depth [21]. Once the actual fluences are determined, the planned dose distributions can be calculated in a forward manner.

### 2.2.1 The pencil beam convolution algorithm

The Pencil Beam Convolution (PBC) algorithm, developed by Storchi and Woudstra in the late 1990's, can be used to calculate the dose distribution for an arbitrary treatment field [22–24]. In general, the absorbed dose to water ($D$) at a point ($x$,$y$,$z$) due to the primary fluence ($F$) is given by the convolution of $F$ with a kernel ($k$) representative of absorbed dose to water for a narrow photon beam:

$$D(x,y,z;F) = \frac{(f+z_{ref})^2}{(f+z)^2} \int_{-\infty}^{\infty}\int_{-\infty}^{\infty} F(x',y')P_{int}(x',y',z)k(x-x',y-y',z)\,\mathrm{d}x'\mathrm{d}y' \tag{2.1}$$

where $P_{int}$ is the intensity profile and accounts for off-axis variation in primary fluence with respect to depth, $f$ is the distance from the source to the surface of the phantom, and $D$ is relative to $z_{ref}$ [24]. An example of the pencil beam kernel used for PBC dose calculations at VIC is shown in Figure 2.4. In this method, both $\mathrm{P}_{int}$ and the pencil beam kernel are derived empirically from linac beam commissioning measurements. The required beam data typically consists of a series of dose profiles measured at various depths for several square field sizes [24]. This method assumes that $P_{int}$ and $k$ are radially symmetric.

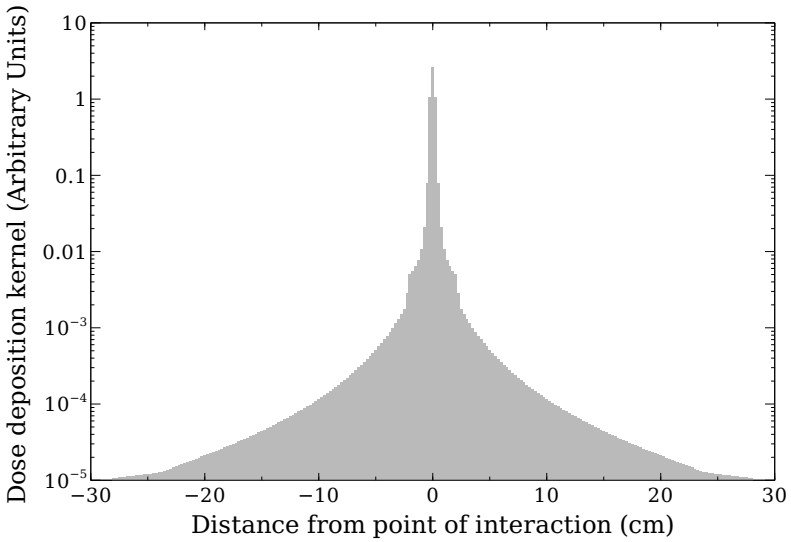


**Figure 2.4:** The pencil beam dose kernel used at VIC for PBC dose calculations. The kernel was derived from commissioning data, and exported from Eclipse.

### 2.2.2 The anisotropic analytical algorithm

The simplicity of the PBC is considered limited in its ability to characterize the primary fluence, scatter kernel and heterogeneities. The Anisotropic Analytical Algorithm (AAA) was developed to address these shortcomings of the PBC. Like the PBC, AAA also considers dose around a narrow pencil beam of photons, but the primary fluence is divided into the contributions of three distinct sources: the primary photon source, the extra-focal photon source and a source representative of contaminating electrons [25, 26]. In this way, each contribution can be independently defined with an individual energy spectrum, fluence, and scatter kernel. The primary fluence is based on a precalculated (MC) energy spectrum of bremsstrahlung in the tungsten target [25, 27]. Agreement between calculation and measured dose profiles is optimized by adjusting mean radial photon energy and radial photon intensity to account for beam hardening (low energy photon attenuation) by the flattening filter. The extra-focal photon source accounts for Compton scatter and bremsstrahlung arising in the components of the linac head (distal to the target). These contribu-

tions to the beam are approximated by a finite source for which the spectrum, size and relative weight are optimized with respect to dose profile measurements, with respect to the penumbra. The electron contamination source which mainly models the contribution of Compton scattered electrons is significant for the accuracy of dose deposited at depths up to approximately 1.5 cm, given the short range of these particles [25]. For a given dose calculation, pencil beam convolutions are performed for each source. This is followed by the superposition of all three independently calculated contributions. Unlike the PBC (which uses empirical kernels), AAA uses an optimized combination of precalculated monoenergetic pencil beam kernels that are weighted according to the optimum energy spectra of each source [27].

A difference map between PBC and AAA calculated dose distributions for a 10x10 $cm^2$ 6 MV field incident on a flat water phantom (with its surface positioned 100 cm from the source) is shown in Figure 2.5. The largest discrepancies in dose

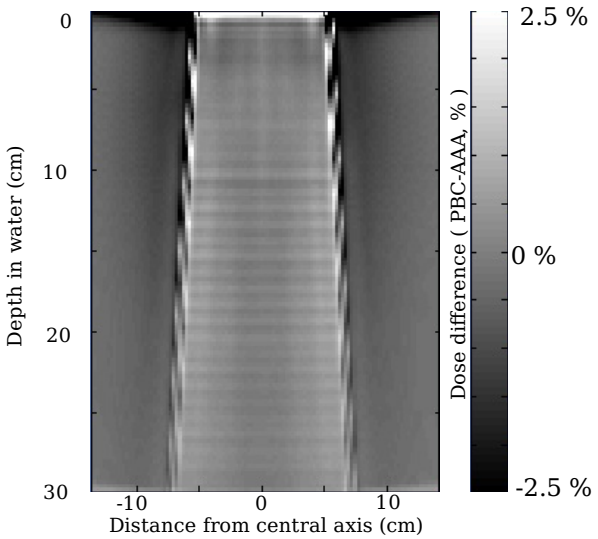


**Figure 2.5:** The comparison between PBC and AAA dose calculations for a square field (Eclipse version 8.6.15, courtesy of K. Bush, 2010 unpublished).

between the two algorithms occur in the build-up region (due primarily to electron contamination differences) and penumbra (where the AAA extra-focal photon source provides greater accuracy).

### 2.2.3 The Monte Carlo method

Monte Carlo (MC) methods are used to calculate dose distributions by simulating, on a statistical basis, the transport of individual particles [28–30]. The interactions of particles with matter are well characterized; however, these quantities are stochastic and analytical solutions are not possible. Instead, MC dose calculations involve sampling the probability density function ($p(x)$) of each stochastic variable (e.g. point of photon interaction, interaction type, Compton scattering angle, etc.) with uniformly distributed random numbers.

Given a probability density function, the random variable can be sampled using uniformly distributed random numbers:

$$\mathrm{G} = \int_0^X p(x)\,\mathrm{d}x \tag{2.2}$$

where G is a uniformly distributed random number between zero and one, and $X$ is the sampled random variable associated with $p(x)$ [30]. To simulate some stochastic process of an interaction, $X$ can be determined by generating a value for G using a random number generator and evaluating the integral. In principle, each interaction of a particle's trajectory (a random variable) can be simulated by sampling the appropriate probability density function. Analytical integration and inversion of the probability density functions is not always possible, and often requires numerical integration . Although the simulation of any one particle is unrevealing, the cumulative result of several primaries is, within a given uncertainty, consistent with the physical process. Based on the stochastic quantities calculated for many transported particles, absorbed dose and other quantities of interest can be computed. The Electron Gamma Shower NRC[2] (EGSnrc[3]) is a library of user codes that generically simulates

[2]National Research Council Canada

[3]The EGSnrc simulation package is an adaption of the more widely spread Electron Gamma Shower (EGS) and specifically designed for use in radiation therapy [31].

the transport of photons and electrons through a medium [32].

BEAMnrc, a user code of EGSnrc, is used to explicitly model the linac compenents. Each component of the linac is designated with appropriate material properties (density, interaction cross sections, etc.) and modeled in a virtual environment. Patient anatomy or a phantom can be reconstructed from CT DICOM images where HU units are converted to physical densities and material types. The path of a particular particle becomes a segmented trajectory divided into parts corresponding to the distances different materials are traversed. The energy dissipated by electrons as they are transported can be scored in terms of absorbed dose.

A variety of techniques have been developed to improve the efficiency of MC dose calculations. One of the least efficient aspects of electron transport is the extensive elastic and inelastic scattering events, whereas the energy and trajectory of the electron is changed only slightly. With the *condensed history technique*, several of these minor interactions are combined in a single step where the particle is transported in a straight line consistent with multiple scattering theory [30]. This technique trades efficiency for accuracy, as it neglects the differences in material characteristics for steps that cross boundaries of the media.

MLC modeling is an important aspect of the MC calculations of IMRT. At VIC, MLC modeling is performed using the particle DMLC code [33]. Using this method, MLC geometry is explicitly modeled, including the rounded leaf-tip and the tongue and groove-shaped leaf edge. For each field, particles are transported through the MLC in the following way: First, the set of MLC apertures, described by the MLC positioning file, is linearly interpolated to 10000 apertures in such a way that each aperture is weighted equally. This set of apertures more accurately describes the MLC movement taking place between control points during delivery. Next, simulated photons exiting the secondary collimator are individually transported through a randomly selected MLC aperture. For each simulated photon, the probability that

it will not interact with the MLC is given by $e^{-\mu(E_\gamma)x}$, where $\mu(E_\gamma)$ is the linear attenuation coefficient of tungsten for a photon of energy $E_\gamma$, and $x$ is the distance of tungsten traversed by the photon. Individual photons are statistically weighted by the corresponding probability of not interacting and recorded at a plane down-beam of the MLC. Last, statistical measures are taken to increase the efficiency of the calculation. These include a technique called Russian Roulette, whereby lightly weighted photons are combined and transported as a single heavily weighted photon. In addition, explicitly simulating the production of Compton scattered photons requires an inefficient number of primaries. For this reason, Compton scattered photons are forced to be produced for each simulated photon and attributed a relatively small statistical weight, accordingly.

## 2.3 Patient-specific QA for IMRT

The safe and effective delivery of IMRT requires a patient-specific quality assurance program. A variety of verification measurement techniques are used by different institutions, and no standards have yet been implemented [34]. One aspect of such a program is the verification of the planned dose distribution. Routine IMRT QA programs usually involve creating a *verification plan*, whereby the fluences of an IMRT treatment are recalculated on a water phantom. The accurate delivery of the planned dose distribution dose is then verified by measurement, indirectly verifying that the treatment plan will be successfully delivered. A selection of dosimeters are used for this purpose, including ion chambers, films, and Electronic Portal Image Devices (EPIDs).

### 2.3.1 Verification measurement techniques

#### Ion chamber point dose measurements

Ion chambers are widely used in the field of radiotherapy dosimetry [8, 35]. Dosimetric verification measurements can be made with an ion chamber positioned inside an

appropriate phantom. The Wellhofer IC15 (Wellhofer Dosimetrie, Schwrazenbruck, Germany) is a typical thimble-type cavity ion chamber used for IMRT verification measurements at VIC, and is illustrated in Figure 2.6. When the ion chamber is

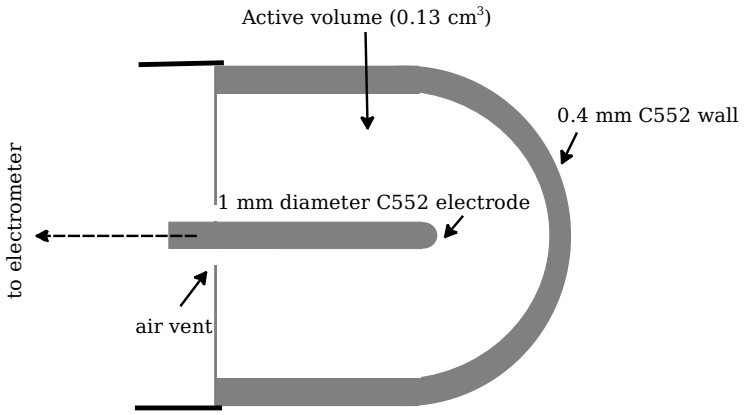


**Figure 2.6:** Schematic profile view of The Wellhofer IC15 ion chamber. Ion pairs produced as a result of incident ionizing radiation in the air cavity are collected by applying an electric potential between the wall and the electrode, recorded as a current by a connected electrometer.

positioned in a field of ionizing radiation, ion pairs produced in the active chamber volume of air can be collected by applying a voltage (typically 200-500 V) between the chamber wall and the electrode. The wall and electrode of the Wellhofer IC15 are made of air-equivalent material (C552), preserving favourable dosimetric similarities between air and water.

Dosimetry using ion chambers requires proportionality between the amount of ionization and absorbed dose at the location of measurement. This condition is described as Transient Charged-Particle Equilibrium (TCPE), and refers to the situation where the energy fluence of ionizing particles leaving a specific location is replaced by a proportionate amount. For indirectly ionizing radiation, TCPE is achievable at depths greater than the maximum range of the secondary electrons. In the event of no gradient in energy fluence, the condition is termed Charged Particle

Equilibrium (CPE).

Provided with CPE, the absorbed dose to the gas ($D_g$) is given by

$$D_g \overset{\text{CPE}}{=} \frac{Q}{m}\left(\frac{\overline{W}}{e}\right)_g \tag{2.3}$$

where $Q$ is the charge collected, $m$ is the mass of the air in the volume, and $\left(\frac{\overline{W}}{e}\right)_g$ is the mean energy required to produce an ion pair in air per unit charge. For therapeutic energies, $\left(\frac{\overline{W}}{e}\right)_g$ can be considered to be a constant and independent of the energy of the ionizing radiation. In the case of TCPE, the equality in Equation 2.3 becomes a proportionality and is equally useful for relative dosimetry. The absorbed dose to water ($D_w$) is related to $D_g$ by the mean stopping power[4] ratio of water to air $\left(\frac{\overline{L}}{\rho}\right)_g^w$,

$$D_w = D_g\left(\frac{\overline{L}}{\rho}\right)_g^w \tag{2.4}$$

The ratios between the restricted stopping powers of air and water are approximately constant over the range of therapeutic energies [8]. In turn, ion chamber dose measurements are independent of photon energy and proportional to dose.

Verification using ion chamber point dose measurements may be supplemented with additional measurements, such as film to provide 2 -dimensional dose profiles [36]. Although film is versatile and has an incomparably high resolution, the benefits are weighted against high energy dependence, costly development, inter-batch/intra-batch variability and setup time.

**EPID measurements**

Planar 2-dimensional fluence measurements called *portal images* are used to verify patient positioning and verify delivered dose [34]. Portal images can be electronically recorded by an Electronic Portal Imaging Device (EPID); a flat panel detector that

[4]Stopping power refers to the average energy loss of a particle per unit path length.

records images with pixel intensity relative to dose. The EPID used at VIC is a Varian aS500 amorphous silicon (a-Si) device (Varian Medical Systems, Palo Alto, CA, USA) connected to the gantry of the Varian Clinac 21EX via a retractable arm. When extended, the surface of the EPID is positioned facing the linac source. The EPID has a 40x30 $cm^3$ active surface area, composing an array of a-Si photodiodes (512x384 pixels, pixel pitch = 0.784x0.784 $mm^2$) [37].

The aSi photodiode is most receptive to electromagnetic radiation in the visible spectrum, and inefficiently responds to megavoltage photons [38]. For this reason, components of the aS500 convert the incident radiation to visible light, involving a two-step process [37]. First, secondary electron fluence is amplified with a 1 mm thick copper build-up plate. Second, secondary electrons proceed to a 0.5 mm phosphor screen of gadolinium oxysulphide, producing a dose proportionate amount of visible light by phosphorescence. The configuration of these EPID components is shown in Figure 2.7.

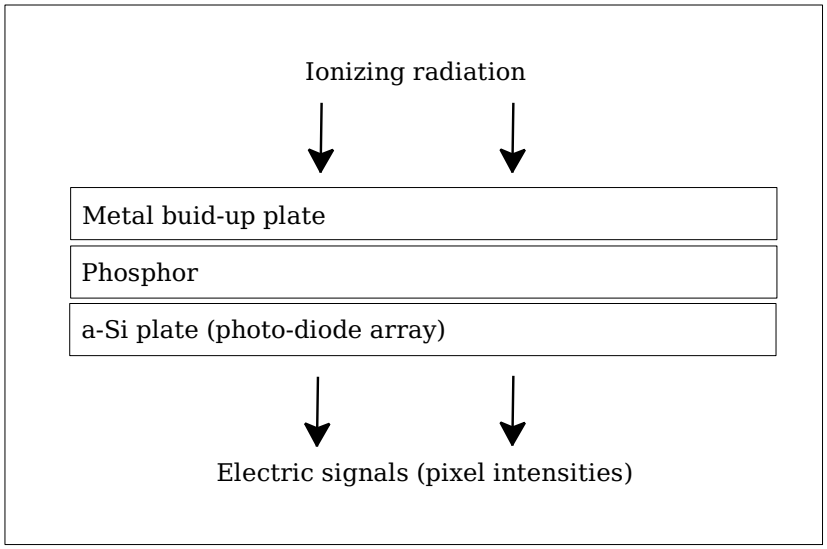


**Figure 2.7:** The configuration of aSi EPID components.

Each photodiode of the EPID is itself a relative dosimeter and representative of one pixel in an Electronic Portal Image (EPI). The photodiodes act as capacitors that

collect and integrate the charge liberated by exposure to light, measured electronically at a later time [38]. EPIs are recorded by averaging frames to prevent saturation of the photodiodes (acquired every 0.125 seconds at 400 MU/min) [37]. Calibration requires that a dark current field EPI (DF), a record of pixel response unrelated to exposure, be subtracted from each raw EPI ($I_{\text{raw}}$); additionally, each pixel of an EPI must be normalized by the EPI of an open flood field (FF) to account for individual pixel response [37]. The calibrated EPI ($I$) is given by:

$$I = \frac{I_{\text{raw}}(x,y) - \text{DF}(x,y)}{\text{FF}(x,y) - \text{DF}(x,y)}[\text{FF}(x,y) - \text{DF}(x,y)]_{\text{mean}} \tag{2.5}$$

Greer *et al* showed that the inherent build-up materials of the aS500 EPID were sufficient for the accurate dosimetry of 6 MV static field photon beams [37]. aSi EPID response has been shown to be linear with dose rate and integrated dose. A slight field size dependence has also been observed[5], attributable to the higher proportion of scatter in larger fields. Since the scatter has a lower mean energy, the high Z components of the EPID phosphor screen will over respond[37]. EPI normalization by the FF completely removes off-axis variation. However, this deficiency can be compensated for by appropriately applying previously measured off-axis ratios [39, 40].

### 2.3.2 Portal Image-based 3D dose reconstruction

EPID measurements can be used to calculate volumetric dose distributions. EPIs can be converted to fluence for use in MC simulations or TPS calculations, and various independent EPI-based deconvolution/convolution dose reconstruction methods have been developed [17, 41] At VIC, EPI-based three-dimsensional dose reconstruction and subsequent evaluation is done using EPIDose, a MATLAB-based software package developed in-house for the rapid evaluation of IMRT verification plans [17].

[5] A field size dependence of EPID dosimetry has been shown to be as much as 4.5% for fields between 4x4 cm$^2$ and 24x24 cm$^2$ (compared to ion chamber) [37].

Using EPIDose, dose distributions can be reconstructed in a virtual cylindrical water phantom using treatment field EPIs. This technique has been shown to provide a rapid and accurate[6] method of IMRT verification for which the number of required measurements and expense of clinical time are relatively low.

For an EPIDose dose reconstruction, EPIs are captured for each treatment field of a verification plan. Additional correction images are acquired to relate treatment EPI pixel intensities to dose at a given depth, including a FF, a DF and a 10x10 $cm^2$. Treatment field EPI calibration is performed using Equation 2.5. For each treatment field, dose to the mid-plane of a virtual cylindrical water phantom is reconstructed using a series of corrections. This procedure includes convolution of the dose with an empirically derived, spatially invariant scatter kernel that approximates the scatter contribution of a physical phantom. Pixel intensities are converted to absolute dose using a pixel intensity-dose conversion factor determined with the EPI of a 10x10 $cm^2$ field for which the absolute dose to the centre of a cylindrical water phantom has been measured in advance. Further corrections account for off-axis differences and phantom contour. The planar dose is then projected through the phantom using attenuation data for depth correction. By completing this process for each of the fields, the contributions can then be summed to form the composite dose distribution.

### 2.3.3 Evaluation criteria for IMRT verification at VIC

Since 2006, PI-based three-dimensional dose reconstruction (via EPIDose) has been the primary means of IMRT verification at VIC. The differences between calculated and reconstructed dose distributions of an IMRT verification plan are assessed in three dimensions. Large dose discrepancies arising in the penumbra of IMRT dose distributions present a problem for the direct analysis of raw dose differences ($\Delta D_{raw}$). When within certain tolerance values for dose ($D_{tol}$) and distance to agreement ($r_{tol}$),

[6] At the time of benchmarking, EPIDose was shown to agree with ion chamber dose measurements to within 1% ± 1% at the reference point (n=20).

the dose discrepancies at high dose gradient locations are not considered significant to the verification process. Many centres, including VIC, use 3% and 3 mm tolerances for dose and distance to agreement, respectively [34]. Developed by Bakai et al, the $\chi$-factor (or simply $\chi$) is a quantitative evaluation function of dose discrepancies that can be calculated at each point of a dose difference distribution, and takes into account the relative significance of high dose gradients with respect to acceptable tolerance values [42]:

$$\chi = \frac{\Delta D_{raw}}{\sqrt{D_{tol}^2 + r_{tol}^2 |\nabla D|^2}} \tag{2.6}$$

Voxels of the distribution with absolute values less than 1 are said to agree within tolerance. Similarly, a weighted dose difference ($\Delta D$) can be evaluated at each point of the distribution, also accounting for high dose gradients [17]:

$$\Delta D = \frac{\Delta D_{raw}}{\sqrt{1 + (r_{tol}/D_{tol}|\nabla D|)^2}} \tag{2.7}$$

The $\chi$ and weighted dose differences are calculated by EPIDose and their distributions can be viewed as two-dimensional cross sections, in any of three orthogonal orientations[7].

The verification analysis of IMRT treatment plans is primarily based on three quantitative metrics: the percentage of voxels within tolerance ($V_{|\chi|<1}$), the mean (weighted) dose difference ($\overline{\Delta D}$), and the reference dose difference ($\Delta D_{ref}$). Action levels have been established for these metrics and surpassing one or more of those action levels constitutes a failure of the verification process. $V_{|\chi|<1}$ is given by the number of voxels within tolerance ($-1 < \chi < 1$) as a percentage of the total number of voxels evaluated. The action level for $V_{|\chi|<1}$ is 90%. $\overline{\Delta D}$ is the average weighted dose difference (EPIDose - calculation), with a 2% action level. $\Delta D_{ref}$ is the dose difference at a reference point, chosen at the time of verification planning to constitute a point

[7]The calculated dose, EPIDose reconstructed dose, and the unweighted dose difference distributions can also be viewed in EPIDose, using the same graphical user interface.

of high dose (>90% of the prescribed dose) and a location of low dose gradient. The absolute value of reference dose difference ($\Delta D_{ref}$) has been attributed a 3% action level.

For routine IMRT verification at VIC, the outcomes of these verification metrics are calculated for two mutually exclusive regions of the dose distribution: a *high dose region*, defined as all voxels above 80% of the reference dose, and a *low dose region* for which the voxels are between 40% and 80% of the reference dose.

## 2.4 Plan complexity

The complexity of an IMRT field describes the relative degree of intensity modulation. Complexity is attributable to the underlying anatomy as well as parameters of the optimization algorithm, such as the prescribed dose and the dose limits on the OAR [43]. For sliding window dMLC IMRT, smaller average windows are required to produce more complex fluence intensity distributions. For this reason, a larger fraction of the fluence is attributable to MLC transmission and scatter [43]. Moreover, this increases the lower limit of dose to critical structures and may jeopardize approximations made by the LMC, compromising the TPS dose calculation. Early descriptions of IMRT fluence complexity were qualitative, made in terms of leaf trajectories or the frequency and amplitude of simple peak-valley intensity patterns [43].

Some methods have been developed to directly include the expense of increasing fluence modulation into the optimization algorithms. Such methods include beam-space intensity restrictions [44], direct aperture optimization [45], and adaptive diffusion smoothing [46]. Other indices have been devised to purely quantify fluence modulation in a physical way. These methods include the Modulation Index (MI), a measure of instantaneous variation in fluence maps, and most recently, the Modulation Complexity Score (MCS) which is an index of MLC aperture geometry variation

[47].

### 2.4.1 The Modulation Index

In 2003, Webb introduced the Modulation Index as a method for quantifying the degree of fluence modulation for 1-dimensional intensity modulated fields [48]. This metric was developed, in principle, to establish a relationship between dose delivery accuracy and the fluence modulation of the contributing fields. MI was shown to quantify the higher complexity of IMRT fields, with respect to few-segment IMRT (fsIMRT) and conformal radiation therapy (CRT). Moreover, MI correlated with the relative dose conformality of these techniques[8].

For a given row (1 to $n$) of elements (or *bixels*) of intensity, $I$, MI is calculated in the following way: The number ($N$) of differences between adjacent bixels ($\Delta I_i = \mid I_i - I_{i+1} \mid$) exceeding a certain fraction ($f$) of the row's standard deviation ($\sigma$) are counted as a function of $f$: $N(f \mid \Delta I_i > f\sigma)$, for $f = 0.01, 0.02...\ 2$. Dividing the $N(f)$ by the number of adjacent bixel pairs (n-1) gives the spectrum $Z$ (Equation 2.8), as a function of $f$:

$$Z(f) = \frac{N(f|\Delta I_i > f\sigma)}{n-1} \tag{2.8}$$

In this way, spectra from all bixel rows of a fluence map can be generated and averaged to give a mean 1-dimensional spectrum ($\overline{Z(f)}$) for the entire array of intensity elements. The corresponding MI is defined as the integral of Z from $f_{min}$ to the upper integration limit ($F$):

$$\mathrm{MI} = \int_0^F Z(f)\,\mathrm{d}f \tag{2.9}$$

This provides a single numerical index for 1 dimensional fluence modulation. Webb suggested that $F$ be equal to 0.5.

This calculation has been extended to 2-dimensions by Nicolini *et al* [49]. In doing

[8] conformality is measured as the ratio of mean dose to the OARs and mean dose to the PTV.

so, the spectrum was redefined as an average over 2 orthogonal components ($Z_x$ and $Z_y$), as well as, a spectrum calculated from diagonal bixel sequences ($Z_{xy}$):

$$Z(f) = \frac{Z_x + Z_y + Z_{xy}}{3} \tag{2.10}$$

Integrating $Z$ with respect to $f$ using $F = 1$ was defined as the 2-dimensional Modulation Index ($\mathrm{MI_{ave}}$). This metric was shown to adequately quantify a selection of fluences that had been smoothed by various amounts. IMRT fields –averaged over multiple sites[9]– were found to have an MI of $18 \pm 4$ ($\mu \pm \sigma$)[10].

[9]This refers to an average MI for multiple plans of 3 planning sites: base-of-tongue, mandible, and left thoracic wall

[10]Consistent with VIC IMRT planning practices, *S50* smoothing of the optimal fluence had been performed by the TPS.

# Chapter 3

# Methods & Materials

A set of IMRT verification measurements were repeated in order to assess the impact of measurement uncertainty on EPIDose verification outcomes. A number of clinical IMRT verification failures at VIC were identified and redelivered to test whether or not the failures were reproducible. Ion chamber measurements were made for consistently failing verification plans to be compared with the planned and EPIDose reconstructed doses. The dependence of verification outcomes on the calculation algorithm was investigated by repeating the PBC dose calculation using AAA and MC. In evaluating the impact of plan complexity on verification outcomes, the fluence modulation of a subset of verification plans was quantified.

## 3.1 Re-evaluation of clinical failures

### 3.1.1 Reproducibility of dose reconstruction measurements

The clinical verification of all IMRT plans had been performed using a single 3-dimensional portal image-based dose reconstruction. In this process, the dose was reconstructed from EPID measurements acquired during delivery of the verification plan, and was therefore subject to measurement uncertainty. Additional sources of uncertainty included variability of the linac output and of the delivery process. The amount of uncertainty, and consequently the reproducibility of the resulting

verification outcomes, was not known. Furthermore, there was no reason to assume that the variability of the process did not change over time, possibly as a result of the mechanical degradation of its components (such as the linac or the EPID, etc.). For IMRT verification to have been effective in distinguishing problematic plans, based on a single delivery, the inherent variability of the verification process was required to have been small relative to the clinical action levels. In order to confidently identify reproducibly problematic IMRT verification plans, the relative importance of statistical delivery and measurement uncertainty to the verification process required evaluation.

Reproducibility of the verification process was assessed in terms of the standard deviation in outcomes for a set of repeated deliveries. In order to assess the variability of an individual verification plan's dose reconstruction EPIs, Two IMRT verification plans were selected and delivered eight times. In an attempt to choose plans representative of the process, one pass and one failure of clinical IMRT verification were selected for repeated delivery. The delivery routine that was used to assess intra-day and inter-day variability is shown schematically in Figure 3.1. Intra-day variability was determined using 8 immediately consecutive measurements, while inter-day variability was measured using 8 once-daily measurements. Each individual dose reconstruction was performed using unique portal images from the delivery of a calibration field-set (composed of the flood, dark current, and 10x10 $cm^2$ fields) and the treatment field EPIs captured immediately afterwards. Inter-linac variability was assessed by performing the same set of measurements for both the primary and secondary treatment linac used for IMRT at VIC.

All EPID measurements required for each PI-based dose reconstruction were generally performed in the same way. This procedure was consistent with the clinical practice of IMRT verification at VIC. The acquisition of the EPIs was made using a Source to Image Distance (SID) of approximately 110 cm using the optical ruler of

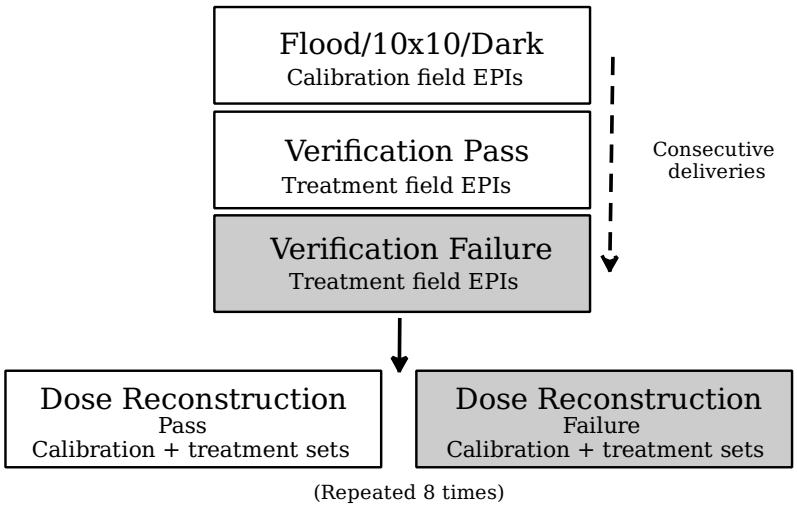


**Figure 3.1:** The delivery routine for the EPID measurements used to assess the reproducibility of dose reconstruction EPIs. As depicted, the dose reconstruction for both verification deliveries were completed using the same calibration field set, recorded immediately prior to both treatment fields.

the linac head[1]. With the EPID in place, three calibration fields were captured prior to the treatment fields; a flood field, a 10x10 $cm^2$ dose calibration field, and a dark field. The flood field EPI was collected for the delivery of 30 MU at 400MU/min uniformly irradiating the active area of the EPID (Y1 = 17 cm, Y2 = 10 cm, X=37.4 cm, GA = 0°, CA = 0°)[2]. This was followed by capturing an EPI for a 40 MU 10x10 $cm^2$ field, also delivered at 400 MU/min, for which dose to the midpoint of a 10.2 cm radius cylindrical water phantom had been previously determined to be 30.8 cGy. This had been accomplished using on ion chamber at the time of commissioning the EPIDose software. The pixel response of the EPID in the absence of ionizing radiation was recorded as the dark current EPI. Once the calibration field set had been recorded, the same EPID setup was maintained while EPIs were captured for all of the treatment fields. Each of these fields was delivered to the EPID from the

[1]In EPIDose, the SID was determined geometrically from the calibration field set.

[2]Before delivery, the EPID position was adjusted longitudinally and laterally so that the entire flood field would be captured by the active region, and was determined using the linac collimator light field.

originally planned gantry angle.

### 3.1.2 Failure identification and re-measurement

Whether or not the failures would consistently fail over time was unknown. Discrepancies between planned and reconstructed dose distributions may have been caused by time-dependent errors of delivery and measurement, and not inherent to the plans themselves. In this respect, it was important to distinguish failures localized in time from plans that consistently fail over time.

Clinical outcomes for the 30 IMRT verification failures occurring between January 2006[3] and October 2009 (inclusive) are summarized in Table 3.1. In all cases, failure was restricted to the high dose region and outcomes for the low dose region were generally very good. A retrospective analysis of these results began with confirming these measurements by repeating the dose reconstruction EPI measurements for each plan, essentially reenacting the verification procedure experimentally. For consistency, the analysis of clinical failures was restricted to IMRT verification outcomes recorded before late October 2009, when the Eclipse treatment planning software (version 8.1.18) was upgraded to version 8.6.15. All plans that failed verification criteria based on these new measurements were reclassified as *consistent* failures.

### 3.1.3 Ion chamber measurements

For those plans consistently failing the verification process, the reason for failure was not known, but the causes for those dose discrepancies were considered to be inherent to the plans themselves. Delivery errors, measurement uncertainty, and inaccuracies of the treatment planning dose calculation algorithm were all potential reasons for the undesirable verification outcomes. If the dose reconstruction was accurately capturing delivery errors, a second measurement was required to confirm the problematic delivery. If delivery errors had not occurred, agreement between the

[3]Since January of 2006, VIC has adopted the Epidose dose reconstruction technique for conducting all IMRT patient-specific QA.

**Table 3.1:** Summary of clinical IMRT verification failures, listed in chronological order. Verification outcomes exceeding the clinical action levels are shaded in gray.

| Plan # | Date of QA | Prescribed dose | Disease site | Reference point | High dose region ($EPI - Ecl$) | |
|---|---|---|---|---|---|---|
| | mm/dd/yyyy | cGy (fraction) | | $\Delta D_{ref}$ (%) | $-1 < \chi < 1$ (%) | $\overline{\Delta D}_{EPI-Ecl}$ (%) |
| 1 | 03/02/2006 | 6000 (25) | L base tongue | 0.9 | 88.9 | 0.4 |
| 2 | 05/05/2006 | 6000 (25) | BOT | -3.3 | 94.0 | -0.9 |
| 3 | 05/19/2006 | 5000 (25) | Antrum | 0.1 | 83.2 | -1.0 |
| 4 | 05/25/2006 | 6000 (25) | Larynx | -2.1 | 82.1 | -1.7 |
| 5 | 06/13/2006 | 6000 (25) | Palate | -2.7 | 88.0 | -1.1 |
| 6 | 06/19/2006 | 6000 (25) | Tongue | -2.8 | 83.1 | -1.5 |
| 7 | 11/09/2006 | 6000 (25) | BOT | -2.1 | 81.4 | -1.6 |
| 8 | 05/02/2007 | 6000 (25) | H & N | 2.1 | 89.5 | 1.4 |
| 9 | 05/09/2007 | 4500 (20) | Thyroid | -2.3 | 89.9 | -1.7 |
| 10 | 11/07/2007 | 6000 (25) | Larynx | -1.8 | 88.8 | -1.8 |
| 11 | 02/26/2008 | 7000 (35) | H & N + Nodes | 2.0 | 86.9 | -0.3 |
| 12 | 02/29/2008 | 7000 (35) | H & N + Nodes | 0.4 | 83.6 | -1.5 |
| 13 | 05/22/2008 | 7000 (35) | Tongue | -0.6 | 87.8 | -1.5 |
| 14 | 06/19/2008 | 6000 (25) | BOT | 2.3 | 88.2 | 1.3 |
| 15 | 08/07/2008 | 7000 (35) | Oropharynx | 1.6 | 98.7 | 2.1 |
| 16 | 08/07/2008 | 7000 (35) | R Tonsil | 2.5 | 96.8 | 2.3 |
| 17 | 09/25/2008 | 7000 (35) | Tongue | -1.2 | 79.0 | -2.1 |
| 18 | 10/06/2008 | 7000 (35) | BOT | -3.1 | 83.3 | -1.8 |
| 19 | 10/31/2008 | 5220 (29) | Meningioma | -4.9 | 91.1 | -1.6 |
| 20 | 01/29/2009 | 7000 (35) | Oropharynx | -1.3 | 88.7 | -1.7 |
| 21 | 01/30/2009 | 6000 (25) | Tongue | -2.6 | 88.5 | -1.5 |
| 22 | 03/05/2009 | 7000 (35) | Oropharynx | 3.4 | 65.7 | 2.4 |
| 23 | 03/16/2009 | 5500 (20) | Oral Cavity | -3.8 | 68.3 | -2.4 |
| 24 | 04/02/2009 | 6000 (25) | BOT & Esophagus | -1.5 | 76.6 | -1.7 |
| 25 | 06/15/2009 | 7000 (35) | BOT | -5.1 | 70.8 | -2.3 |
| 26 | 06/15/2009 | 6000 (25) | RMT | -3.9 | 78.6 | -1.8 |
| 27 | 06/17/2009 | 7000 (35) | Lt.Tonsil | -1.5 | 81.1 | -1.8 |
| 28 | 07/14/2009 | 7000 (35) | BOT | -1.9 | 87.7 | -1.6 |
| 29 | 08/24/2009 | 3500 (15) | Thyroid | -0.1 | 79.1 | -2.0 |
| 30 | 10/02/2009 | 7000 (35) | Oropharynx | -1.3 | 88.0 | -1.4 |

two measurements suggested that the dose calculation algorithm was contributing significant errors to the dose discrepancies. Alternatively, agreement between the independent measurement and the planned dose distribution would have indicated that some aspect of the delivered plan had compromised the PI-based dose reconstruction process. In principle, accurate and trusted measurements independent of the dose calculation algorithm of the TPS and the EPIDose reconstruction technique could have been used (in part) to identify reasons for consistent verification failures.

The gold standard for radiation dosimetry, the ion chamber point dose measurement, was chosen as an independent dosimeter for the evaluation of verification failures. Ideally, an ion chamber measurement would have been taken at the reference point for all failures. However, the location of the ion chamber measurement was restricted to the centre of the cylindrical water phantom, which was not necessarily coincident with the reference point, nor was it even at a high dose, low dose gradient

position of the dose distribution. For this reason, the phantom was repositioned with respect to the IMRT fields to ensure the ion chamber was in a region of high dose and low dose gradient, which entailed recalculating dose for each plan.

For each plan that was deemed a consistent failure, the verification fields were repositioned on the phantom image set and a new dose distribution was calculated using that plan's original treatment fields (Eclipse 8.1.18). This was done manually and iteratively until dose to the phantom's centre was above 90% of the prescribed dose, and was uniform to 1% within ±3 mm in all of three orthogonal directions. This criteria was chosen to ensure the point of ion chamber dose measurement be representative of a clinically acceptable reference point, coinciding with previous verification practice. The centre of the phantom for these repositioned plans was thereby considered a suitable location for comparing ion chamber point dose measurements, reconstructed point dose measurements and the calculated dose.

The re-calculated dose distributions were delivered with the physical phantom and the ion chamber positioned at the planned location, and dose measurements were recorded. Individual measurement were made for each treatment field as if it were delivered clinically. Shortly afterwards, portal images for dose reconstructions concerning the same set of deliveries were collected for later comparisons.

A Wellhofer IC15 (IC1) ion chamber (see Section 2.3.1) was positioned at the centre of a 20.4 cm diameter cylindrical water phantom. The entire apparatus was connected to the end of the treatment couch with its axis perpendicular to gantry rotation. Over the course of individual field deliveries, the current collected by the ion chamber was measured and integrated using a PTW UNIDOSE electrometer supplying a 300V bias. The setup for the ion chamber measurements is depicted in Figure 3.2. Given the often non-uniform dose distributions of IMRT verification plans, accurately positioning the ion chamber was essential in limiting a large proportion of the measurement uncertainty. Preliminary positioning of the ion chamber

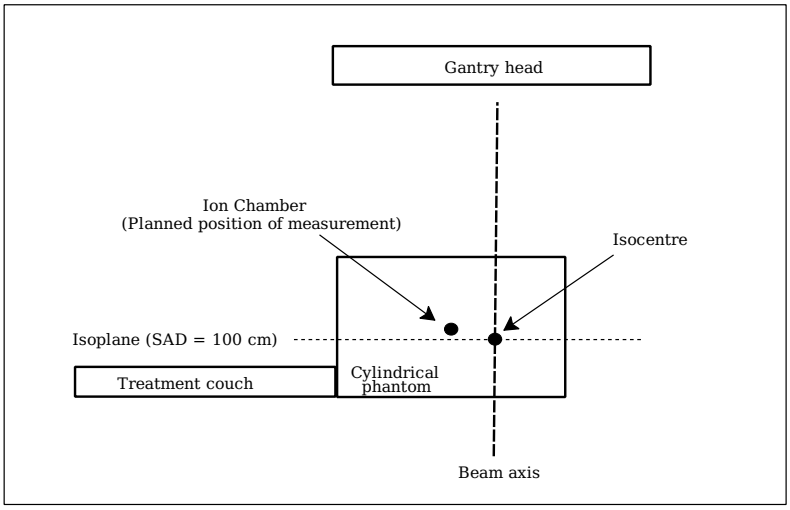


**Figure 3.2:** The experimental setup for an arbitrary ion chamber IMRT verification measurement. The ion chamber was calibrated at the isocentre and then, for each recalculated failure, moved to the location of measurement by moving the treatment couch.

was done using the treatment vault isocentric lasers, accurate to within ±2 mm. Due to the longitudinal asymmetry of the apparatus, the exact longitudinal location of the chamber's enclosed active volume could not be visually identified. Instead, the longitudinal position of the apparatus relative to the isocentre was established by means of a Y1 collimator edge profile. In this configuration, the diameter of the ion chamber would span the field edge and, in principle, measure the average dose of the penumbra when located at the isocentre. This is depicted in Figure 3.3. Using an asymmetric square field (100 MU, Y1 = 0 cm, Y2 = 10 cm , X = 10 cm Col = 0°, GA = 0°), a collimator edge profile was constructed by measuring ion chamber current for a series of longitudinal positions spanning the beam axis. One such profile, normalized to the maximum integral current, is provided in Figure 3.4. The phantom was then positioned using the couch index to within 1 mm of the determined 50% profile location. The phantom was then laterally and vertically repositioned until the integrated current was constant to within 1% for a number of fields (X=10 cm,Y=10 cm, 100 MU) delivered from multiple gantry angles (0°, 90°, 180°, and 270°). Phan-

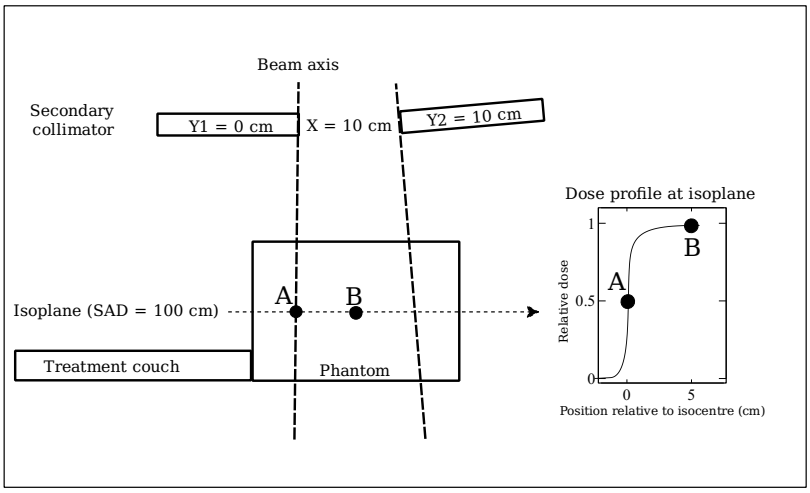


**Figure 3.3:** The method for dosimetric positioning of the phantom for ion chamber verification measurements. In order to accurately position the ion chamber at the isocentre, the appropriate longitudinal location was identified dosimetrically. This assumed a 50% relative dose at the isocentre for a 10x10 $cm^2$ field, delivered with the Y jaw position set to zero 0 cm (Y1 = 0 cm, Y2 = 10 cm X = 10 cm).

tom positioning for IMRT treatment fields delivery was performed using the digital readout of the treatment couch. In this way, ion chamber and phantom positioning were independent of vault laser uncertainties, allowing for more accurate positioning.

With the phantom aligned to the isocentre, a charge-dose calibration factor was determined by comparing the current collected from 100 MU 10-by-10 cm fields (X = 10, Y = 10) to a previously determined 77.0 cGy dose to the phantom's centre for that particular field. An attempt was made to account for any gantry angle dependence and output variation by averaging the response measurements from 8 fields: 100 MU 10x10 $cm^2$ fields (X = 10 cm, Y = 10 cm, Col = 0°) delivered twice from 4 gantry angles (0°, 90°, 180°, and 270°).

For each delivery of a verification plan identified as a consistent failure, the phantom was positioned at the planned phantom coordinates by moving the treatment couch. A single measurement was then made for each treatment field as if it were delivered clinically. Following the ion chamber measurements, portal images for PI-

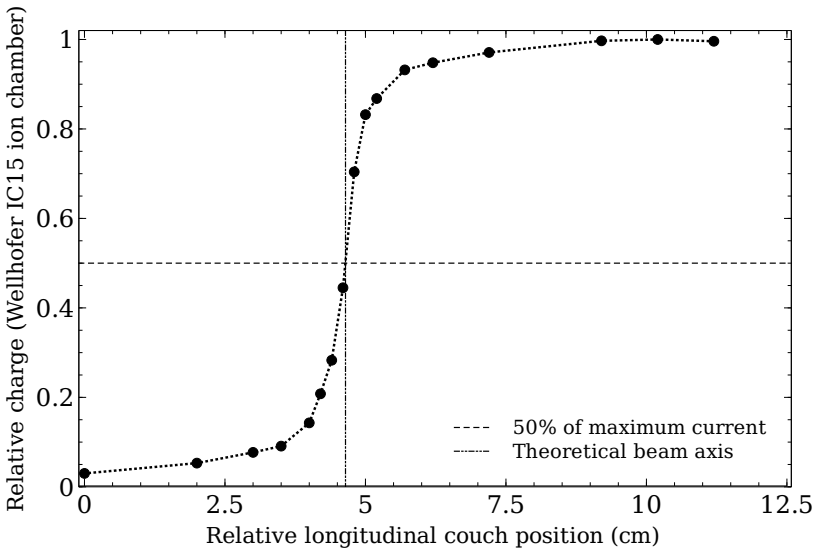


**Figure 3.4:** A collimator edge profile used for dosimetric positioning of the ion chamber at the isocentre. Relative charge (integrated ion chamber current) was recorded along the central axis of the 20.4 cm diameter cylindrical water phantom relative to a collimator positioned over the isocentre (Y1 = 0 cm, Y2 = 10 cm, X = 10 cm).

based dose reconstructions were collected for later comparisons. MLC initializations were performed before delivery of the first plan, as well as after every 2-3 plan deliveries, in order to reduce the possible accumulation of MLC positioning errors associated with several successive deliveries. Since it was not practically possible to deliver all the failure plans in a single evening, the entire positioning-calibration-delivery routine was completed on each measurement day.

## 3.2 Recalculation of planned dose distributions

Inaccuracy of the planned dose distributions was investigated as a possible contributor to the production of IMRT verification failures. The outcomes of verification for all plans were based on dose distributions calculated using the pencil beam convolution algorithm (PBC) (Eclipse 8.1.18). The planned dose distributions of consistent verification failures were recalculated using two advanced calculation engines: the anisotropic analytic algorithm (AAA) with an updated actual fluence calculator (Eclipse 8.6.15), and Monte Carlo (MC). These calculation engines were known to

provide higher accuracy in dose calculations, relative to the PBC. If a verification outcome for a consistent failure were resolved using AAA, this would have suggested that deficiencies in the PBC contributed to the original discrepancy between planned and reconstructed dose. MC was also capable of providing better accuracy than the PBC and was used as a third independent dose calculation for comparing the two algorithms.

### 3.2.1 AAA

For each plan, the original MLC control point sequences and plan parameters were imported into Eclipse in the absence of optimal fluence. Actual fluence for each field was then calculated from the MLC sequences using an upgraded version of the actual fluence calculator (Eclipse 8.6.15). The AAA calculation was performed with a 2.5 mm voxel width on the verification phantom (consistent with the PBC dose calculation). All plan parameters were kept the same as in the clinical verification calculation.

### 3.2.2 Monte Carlo dose calculation

VIC has established a MC dose calculation system for the verification of 6 MV and 18 MV radiotherapy treatment plans, aptly named Vancouver Island Monte Carlo (VIMC). It is a fully automated system designed to accept Eclipse treatment plans exported in DICOM format, and, in turn, generate dose and respective uncertainty distributions packaged in DICOM format for import back into the TPS. User input for the MC dose calculation included a requested statistical uncertainty and voxel size. Verification plans for all consistent failures were recreated using a high resolution phantom (simply to comply with VIMC input specifications) and exported from Eclipse to the VIMC system for Monte Carlo calculation of the dose distributions. The resulting MC dose distributions were then exported from VIMC as a set of DICOM files back into Eclipse, where the MC dose distributions were subsequently

prepared for verification analysis. A statistical uncertainty ($\delta$) of 0.5% voxel dose was requested, and required approximately $10^9$ primaries per field. The number of primaries ($N_\gamma$) required for the desired uncertainty was pre-estimated for each field before simulation using Equation 3.1 [50].

$$N_\gamma = \frac{1}{\delta^2 \mu_{en}^{eff}} \frac{A_{\text{beam}}}{V_{\text{voxel}}} \tag{3.1}$$

where $\mu_{en}^{eff}$ was the effective energy absorption coefficient, $A_{\text{beam}}$ was the area of the fluence, and $V_{\text{voxel}}$ was the voxel volume.

The VIMC dose calculations consisted of 3 fundamental components: linac modeling, MLC modeling, and dose deposition.

**Linac modeling**

The treatment head of the the primary IMRT linac, a Varian Clinac 21EX (Varian Medical Systems, Palo Alto, CA, USA) was simulated using BEAMnrc[4]. It was made to machine specifications outlined in component modules provided by the manufacturer. Monte Carlo simulations of the virtual linac were based on an initial 6.00 MeV monoenergetic electron beam. The radial distribution of the incident electron beam was described by a Gaussian with a full width at half maximum (FWHM) of 0.75 mm.

**MLC modeling**

The MLC was modeled using the DMLC code (described in Section 2.2.3). An additional consideration was that MLC leaf pairs were known to have a minor systematic positioning error, referred to as *backlash*. The magnitude of this error has been shown to be dependent on leaf-pair separation [33]. A systematic change in leaf position of 0.015 cm was introduced to compensate for the backlash. This value has been shown

[4]BEAMnrc is a user code designed for modeling the physical components and geometry of a linac head.

at VIC to provide the best agreement between measurement and MC calculation for sliding window dMLC fields with leaf-pair gaps typical of IMRT fields[5].

**Dose deposition**

MC dose distributions were calculated by simulating the transport of the particles exiting the virtual MLC into and through the phantom. To begin, CTCreate was used to construct a virtual phantom of 2.5x2.5x2.5 cm voxels from DICOM CT images exported from Eclipse. The program DOSXYZnrc simulated the deposition of dose resulting from the incident fluence by calling Monte Carlo routines from the EGSnrc library. Relevant interaction cross-sections can be found in the NRC Technical Report, PIRS-701 [32].

## 3.3 Quantifying the impact of plan complexity

During IMRT treatment planning, the extent of fluence modulation is dictated by the underlying anatomy and dose-volume constraints (on PTV, OAR) used in the optimization of the dose distribution [43]. The possibility of a correlation between consistent verification failure outcomes and plan complexity, quantified in terms of fluence modulation, was investigated. The evaluation of fluences from consistent failures was combined with that from 10 consistently passing verification plans. This was done to obtain a spectrum of verification outcomes that span the respective action levels. Fluence modulation was quantified in terms of average leaf-gap, as well as, the modulation index (MI) and a novel metric derived from MLC aperture geometry.

### 3.3.1 Calculation of the modulation index

The modulation index (as described in Section 2.4.1) was calculated for all consistent failures, and for plans of the consistently passing subgroup. For the purposes of the

[5]Although highly variable, the average leaf-gap of MLC pairs for dMLC IMRT has been shown to be approximately 1-3 cm.

MI calculations only, the collimator angle for all fields of each plan were set to zero before they were exported so that the $Z_x$ components of the spectra corresponded to the direction of MLC motion. Consequently, the spectral component $Z_y$ of a given fluence was forced to be consistently representative of variation perpendicular to MLC motion. As an example, Figure 3.5 shows a fluence with respect to the corresponding directions of its spectral components. MATLAB was used to extract fluences from

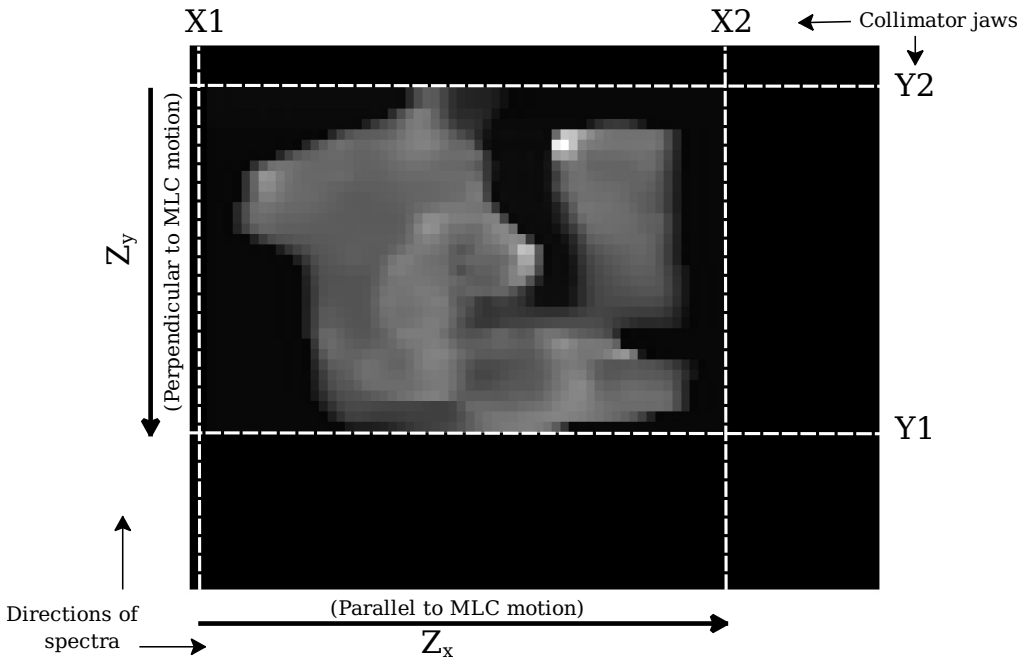


**Figure 3.5:** Orientation of the spectra related to the modulation index calculation with respect to the fluence of an IMRT field. The 1-dimensional spectral components $Z_x$ and $Z_y$ were oriented to represent modulation in directions parallel and perpendicular to MLC leaf motion, respectively. MI was evaluated for the fluence defined by the jaws of the secondary collimator.

RT plan DICOM image files (exported from Eclipse). Pixels were evaluated for a region of the fluence map defined by the jaw positions, rounded to the nearest pixel (defined on a 2.5 mm grid at the isoplane). These calculations neglected the diagonal component of each spectrum because it was not considered to be representative of

**Table 3.2:** Mathematical description of simple intensity maps for testing MI calculation algorithm, where $i$ is the pixel index, $N$ and $\sigma$ are the number of pixels (50) and standard deviation in the fluence, respectively, and $f_{max}$ is the fraction of the standard deviation corresponding to the largest difference possible between adjacent pixels. In each case, $Z_x(f)$ is positive for $0.01 < f \leq f_{max}$ and is zero otherwise.

| Gradient | Fluence ($I$) | $f_{max}$ |
|---|---|---|
| Constant | $I(1:N,i) = i$ | $1/\sigma \approx 0.0686$ |
| Linear | $I(1:N,i) = i^2$ | $\frac{2N-1}{\sigma} \approx 0.1291$ |
| Exponential | $I(1:N,i) = e^{0.1i}$ | $\frac{e^{0.1N} - e^{0.1(N-1)}}{\sigma} \approx 0.3646$ |

any physical parameters[6].

The MI of three simple fluences (shown in Figure 3.6) were evaluated prior to the evaluation of the verification plans. This procedure provided examples to verify the efficacy of the coded MI calculation algorithm. Table 3.2 summarizes each test fluence, and $f_{max}$ for which the spectra is not equal to zero. $Z_x(f)$ and $MI_x(F)$ of the intensity maps were calculated and the results are shown in Figure 3.7.

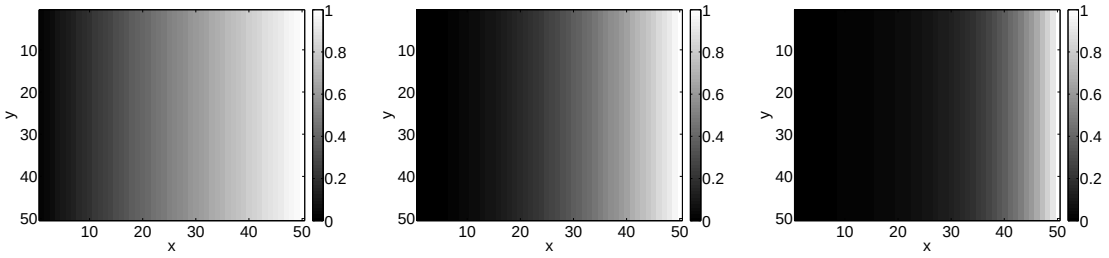


**Figure 3.6:** The simple fluences used for testing the MI calculation algorithm. The variation for each fluence can be described as **(a)** a constant gradient, **(b)** a linear gradient, and **(c)** an exponential gradient.

[6]Using a 2D EPI-based patient-specific QA program, Nicolini *et al* included $Z_{xy}$ because the diagonal variation in fluence maps was considered by the evaluation criteria ($\gamma$) [49].

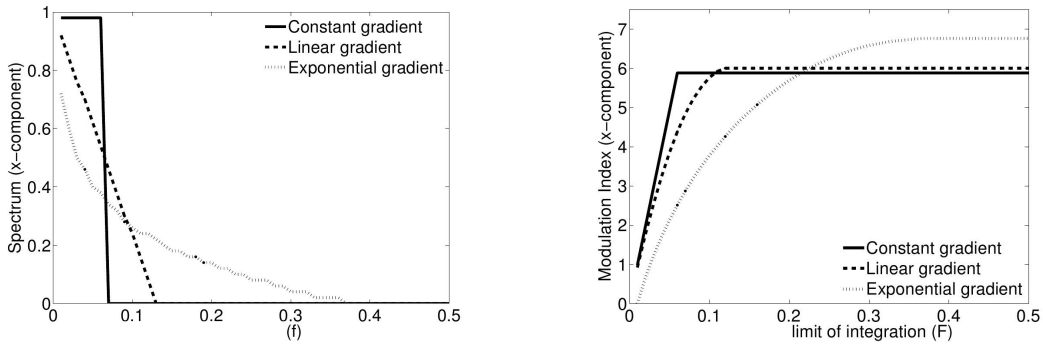


(a) (b)

**Figure 3.7: (a)** The spectral components parallel to the gradients of the 3 simple fluences (see Figure 3.6), and **(b)** the corresponding modulation indices as a function of the upper integration limit, $F$.

**Table 3.3:** An abbreviated summary of the MLC positioning file content and format, where each individual MLC leaf-tip position (relative to the isocentre) is provided for each aperture, $X$. An MU weight ($w$) is provided for each aperture, in terms of the relative proportion of the total MU delivered up to that specific control point.

| Control Point ($k$) | Aperture ($X$) | Relative MU ($w$) |
|---|---|---|
| 1 | $X_1$ | $w_1 = 0$ |
| 2 | $X_2$ | $w_2$ |
| ... | ... | ... |
| N | $X_N$ | $w_N = 1$ |

### 3.3.2 An aperture-based index of plan complexity

An alternative independent metric was defined in order to quantify plan complexity in a simple and novel way: the mean area-perimeter-ratio ($\overline{r_X}$). This quantity was designed to be proportional to the ratio of area and perimeter for the MU weighted average MLC aperture of an IMRT plan. For each plan of interest, information about the dynamic MLC aperture was taken from the corresponding MLC positioning files exported from the treatment planning software. A general representation of a typical MLC positioning file is provided in Table 3.3.

For each control point, the MLC file indicated the position of each MLC leaf

tip, relative to the isocentre. For a given aperture ($X_k$), the area of that aperture ($A_k$) was calculated by summing the separation of leaf pairs and multiplying by leaf width. Similarly, the perimeter ($P_k$) was calculated from the known MLC positions of each aperture. MATLAB was used to compute the relevant quantities associated with aperture, reading in information directly from the MLC positioning files interpreted in ASCII format. The AP-ratio ($r_X$) of each field was then calculated using Equation 3.2,

$$r_X = 4 \sum_{k=1}^{N-1} \frac{A_k}{P_k} (w_{k+1} - w_k) \tag{3.2}$$

where $w$ is the relative MU weight. The ratio is multiplied by a factor of 4 so that the result has a magnitude of 1 cm for a square with the sides of length 1 cm. The average AP-ratio of a plan $\overline{r_X}$ was then calculated as the MU weighted average $r_X$ for all contributing fields (Equation 3.3):

$$\overline{r_X} = \sum_{i=1}^{(\#\text{ of fields})} (r_X)_i \frac{(\text{MU})_i}{(\text{Total MU})} \tag{3.3}$$

# Chapter 4

# Results and Discussion I: Re-measurement of verification failures

The reproducibility of verification outcomes was assessed and described in terms of the standard deviation of repeated measurements. An unforeseen malfunction of the EPID was identified and resolved in this process. Repeated verification measurements for a subgroup of clinical verification failures revealed that several of the clinical outcomes were not reproducible. EPID malfunction, at the time of the clinical verification of these plans, was identified as a possible reason for the original failure. Even after this problem was rectified, a subgroup of plans continuously and for unknown reasons failed the verification process. For these plans, the discrepancies between planned and reconstructed dose distributions were compared to ion chamber point dose measurements. In most cases, the ion chamber dose was between the planned and reconstructed dose, suggesting that both verification planning and verification measurement were contributing in part to the discrepancy. A following analysis of doses associated with the individual fields suggested that the dose discrepancies had accumulated from smaller discrepancies in individual fields.

## 4.1 Reproducibility of dose reconstruction measurements

### 4.1.1 Preliminary assessment of variability

Dose distributions were reconstructed from the EPIs of two plans, one clinical failure and one clinical pass. Variability was assessed for measurements made on consecutive days. The mean verification outcomes of five preliminary inter-day dose reconstructions for each plan are given in Figure 4.1. The standard deviation in the mean dose difference, $\overline{\Delta D}$, of the high dose region for the primary linac was 0.3% (averaged over all 10 measurements). For the same set of measurements acquired using the secondary linac, the standard deviation of $\overline{\Delta D}$ was three times smaller (below 0.1%). Both plans were shown to pass the verification criteria using the primary linac, whereas the clinical failure continued to demonstrate failure using the secondary linac. Combined, the linac dependence of these results indicated that the clinical IMRT verification procedure was in some way compromised, and further diagnostic analysis was required.

### 4.1.2 Diagnosis of dose reconstruction variability

In an attempt to isolate the cause of the higher variability in $\overline{\Delta D}$ for the primary linac, multiple PI-based dose reconstructions were performed for a single set of treatment field EPIs using 5 intra-day calibration field-sets. This was done for both the primary and secondary linacs. This procedure is schematically represented in Figure 4.2. Each calibration field-set was acquired approximately 15 minutes apart, during which time the EPID was under continuous use[1].

Figure 4.3 shows the results for the primary and secondary linacs in terms of mean dose difference of the high dose region for the clinical failure. While the results from the secondary linac were relatively stable, those from the the primary linac varied roughly linearly with time. This resulted in a maximum difference of over 1% in a period of 60 minutes. Given that only a single set of therapy fields were delivered,

[1]Continuous use involved an uninterrupted series of consecutive EPID measurements.

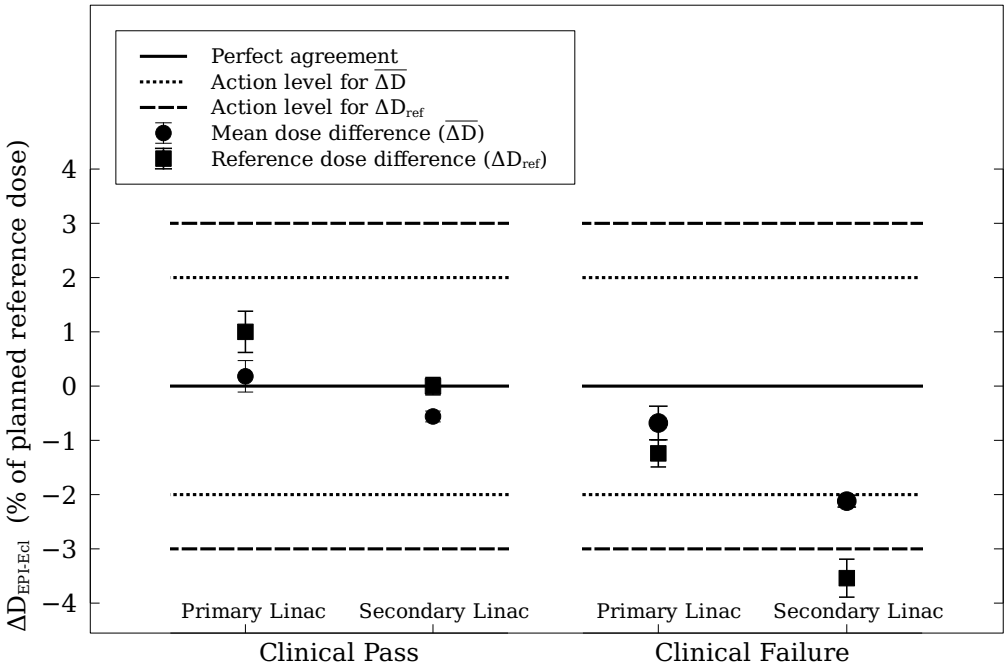


**Figure 4.1:** Mean and reference dose differences between planned (Eclipse 8.1.11) and reconstructed (EPIDose) distributions. The standard deviation in the measurements is shown with the error bars.

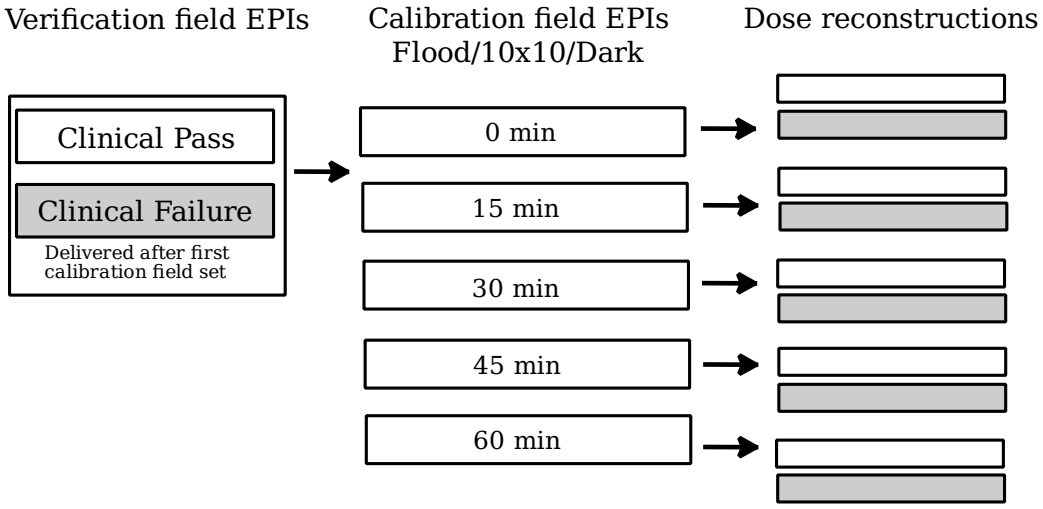


**Figure 4.2:** EPIDose dose reconstruction was performed using multiple calibration field-sets and a single set of EPIs for both the clinical pass and the clinical failure. Pass and failure verification plans were delivered immediately after the first set of calibration fields.

this drift was therefore attributable to how the EPID responded to the calibration fields with time of EPID use.

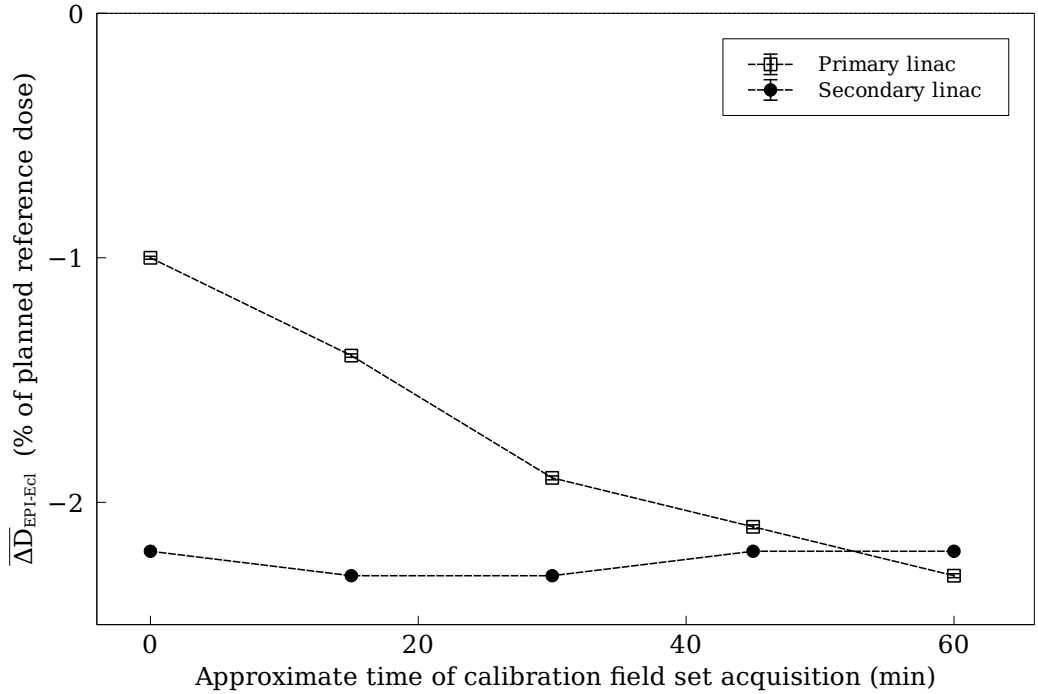


**Figure 4.3:** Mean dose differences ($\overline{\Delta D}_{EPI-Ecl}$), for a series of EPIDose dose reconstructions using calibration field-sets acquired at different times. For completeness, the standard deviation of the mean for each measurement are included as errorbars, although it was negligibly small (less than 1% of the mean).

The behaviour of the EPI for each calibration field of the set (flood, 10x10 cm$^2$, and dark current) was evaluated independently with respect to time, for both linacs. The mean pixel intensity for each flood field was calculated. In addition, the pixel intensity-dose conversion factor derived from each 10x10 cm$^2$ calibration field was recorded. These results, normalized to the highest values, are shown for both linacs in Figure 4.4. The average pixel intensity of five dark current EPID measurements with respect to time is shown in Figure 4.5, again where mean dark current pixel intensity is normalized to the highest value.

With respect to the flood and 10x10 cm$^2$ field EPI measurements, the variability between treatment units over the 60 minutes was roughly equal, and less than 0.1%

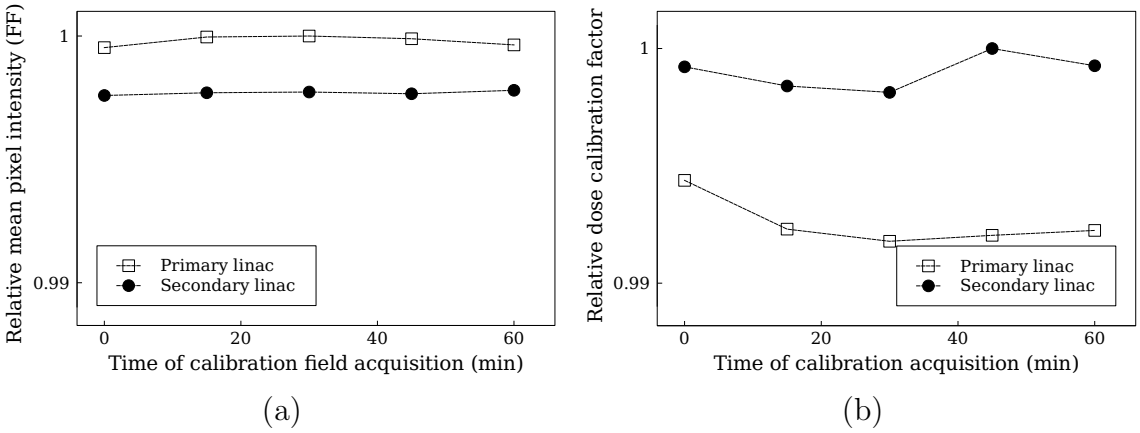


**Figure 4.4:** Relative values for **(a)** the mean pixel intensity of the flood field EPI, and **(b)** the pixel-intensity dose conversion factor, as a function of calibration field-set acquisition time.

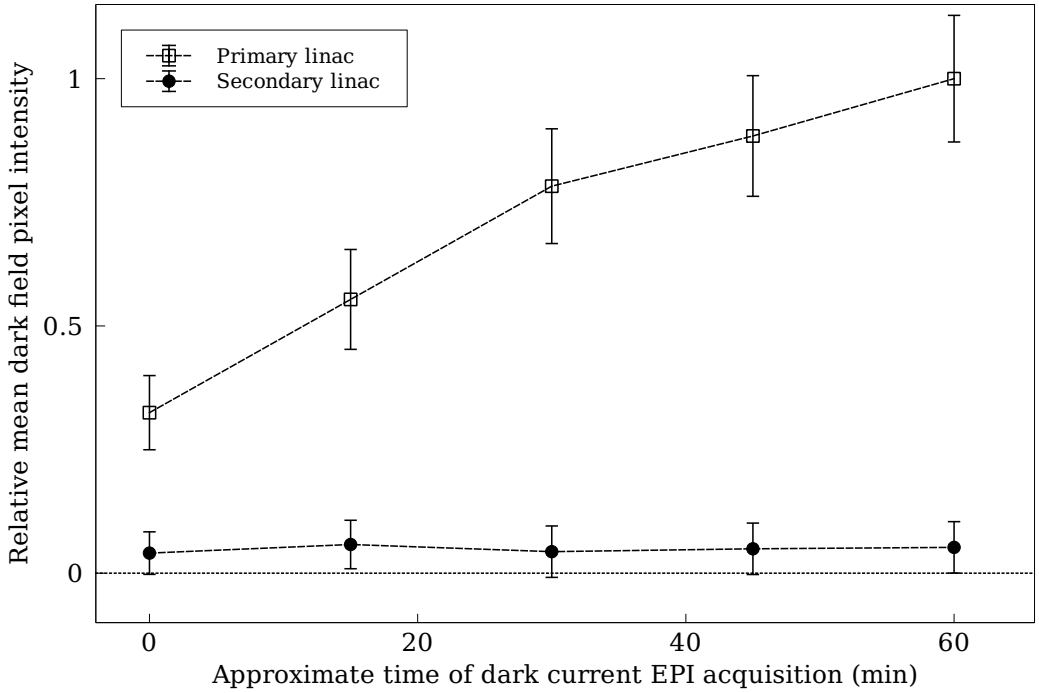


**Figure 4.5:** Mean pixel intensity of the dark current EPI as a function of the acquisition time, for the primary and secondary linac. Mean dark current pixel intensities are normalized to the highest recorded value. Error bars represent standard deviation in normalized dark current pixel intensity.

(standard deviation) in both instances. The variation resulting from the flood fields and 10x10 $cm^2$ calibration fields was therefore not considered to be a contributing factor to the time-dependence of intra-day verification outcomes for the primary linac. The drift in relative dark current of over 60% was presumed to negate the utility of the primary linac EPID as an effective dosimeter and, as a result of this work, the EPID cassette was replaced for that treatment unit.

The same measurements described in Section 4.1.2 were repeated using the new EPID cassette. As shown in Figure 4.6, similar variability in dark current and mean dose difference was observed for both linacs. The mean dose difference determined using the secondary linac was on average 0.6% lower than for the primary linac, and this was not attributable to variability in the calibration field-set.

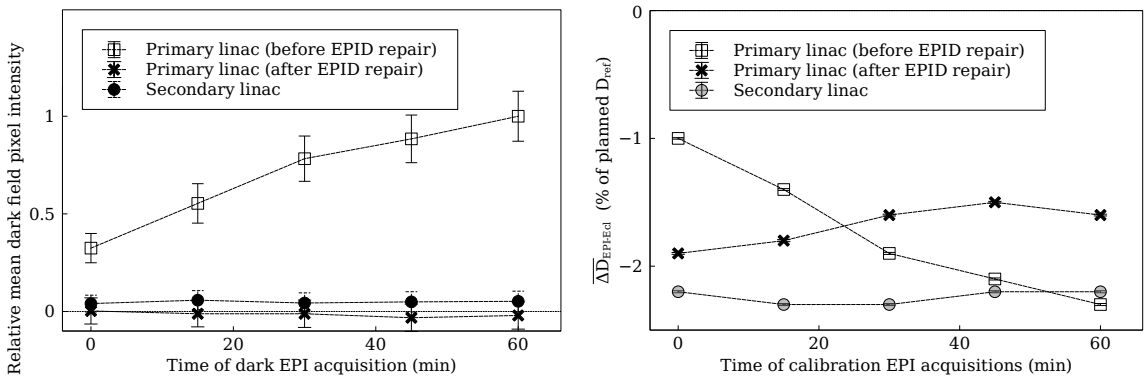


**Figure 4.6:** After the EPID cassette was replaced for the primary linac, the previously observed drift in primary linac EPID response was eliminated and closely approximated the response of the secondary linac, in terms of **(a)** the mean pixel intensity of the dark current EPI and **(b)** the resulting mean dose difference of the high dose region.

### 4.1.3 Summary of reproducibility measurements

Satisfied that the EPID of the primary linac was functioning properly, reproducibility of the PI-based dose reconstruction measurements were re-evaluated using the methods presented in Figure 3.1. In Table 4.1, the intra-day and inter-day reproducibility is summarized in regards to the standard deviation of each set of verification out-

**Table 4.1:** The reproducibility of EPIDose dose reconstructions measured in terms of the standard deviation of verification metrics. 8 measurements were considered for both intra-day and inter-day evaluations. For each verification plan (pass or fail), each dose reconstruction was performed using a unique calibration field-set that preceded it.

| Linac | Plan | Inter-day (%) | | | Intra-day (%) | | |
|---|---|---|---|---|---|---|---|
| | | $\sigma_{\Delta D_{ref}}$ | $\sigma_{\chi}$ | $\sigma_{\Delta Dmean}$ | $\sigma_{\Delta D_{ref}}$ | $\sigma_{\chi}$ | $\sigma_{\Delta Dmean}$ |
| primary | pass | 0.3 | 0.7 | 0.1 | 0.1 | 0.1 | 0.1 |
| | fail | 0.4 | 2.9 | 0.1 | 0.1 | 1.1 | 0.1 |
| secondary | pass | 0.4 | 0.3 | 0.1 | 0.1 | 0.1 | 0.1 |
| | fail | 0.4 | 4.1 | 0.1 | 0.1 | 2.0 | 0.1 |

comes. Concerning the variability of the reference point dose and the mean point dose, no significant difference was observed between linacs. Intra-day variability of these metrics was approximately 0.1% or less, while the inter-day standard deviation of reference dose difference and mean dose difference measurements were 0.4% and 0.1%, respectively. These results were encouraging because they suggest that the variability of the EPIDose reconstruction technique for IMRT verification was approximately one order of magnitude smaller than the tolerances used to make clinical decisions. In other words, with a properly functioning EPID, the inherent variability of the EPIDose reconstruction technique did not significantly contribute to the appearance of verification failures[2].

In addition to showing that there was an equal variability in verification measurements between linacs, these measurements demonstrated that $\overline{\Delta D}$ for the secondary linac was systematically lower than for the primary linac by an average 0.3%. In turn, these differences in response demonstrated the sensitivity of the variability in chi distribution ($\sigma_{\chi}$) to the value of $\overline{\Delta D}$, also summarized in Table 4.1. This meant that a verification pass evaluated with the primary linac may have been identified as

[2]Possible exceptions are reserved for those verification dose measurements that are close to the action levels.

a failure using the secondary linac, and vice-versa. The difference in outcome with respect to the treatment linac used for the verification must therefore be considered to ensure that meaningful clinical decisions are made in the future.

### 4.1.4 The re-measurement of clinical failures

Thirty clinical failures had been identified (see Table 3.1). The verification measurements for these plans were repeated in order to determine if clinical failures would consistently fail. Clinical failures were re-measured using the primary linac, for two reasons: firstly, these measurements were more representative of the clinical situation[3], and secondly, this ensured the consistency of verification outcomes with consideration to the systematic measurement differences between linacs. Although the re-measurement of all 30 clinical failures was attempted, 9 of those plans were not suitable for redelivery. In these instances, the original plan had been overwritten, or the dose distribution had been deleted permanently.

Six of the nine undeliverable verification plans were the failures identified in the first 6 months of EPID based verification at VIC. These plans represented a relatively large frequency of verification failure at VIC during the first 6 months of using portal image-based dose reconstruction for IMRT QA; however, multiple revisions were made to the dose reconstruction technique over this time, such as, the modification of the virtual phantom geometry, and the technique was still largely experimental. For this reason, these clinical failures might not be expected to continue failing under current conditions, and were considered to be of relatively much lower importance.

Verification of the remaining 21 plans was repeated in order to determine if the failure was reproducible. The resulting verification outcomes were considered to be consistent to within the variability outlined in Table 4.1, and are summarized in Table 4.2. Of the re-evaluated clinical failures, ten passes were observed. Two primary explanations of the clinical failure of these plans were identified: First, the

[3]Over 90% of IMRT verifications are performed using the primary linac.

**Table 4.2:** The verification outcomes of the re-evaluated clinical failures. 9 plans could not be re-evaluated, and this subgroup of plans was primarily composed of clinical verifications taking place before 2007. Verification outcomes exceeding the clinical action levels have been shaded in gray.

| Plan # | Date of QA | Outcome | Reference point | Voxel doses > 80% prescribed dose | |
|---|---|---|---|---|---|
| | mm/dd/yyyy | (if measured) | $\Delta D^{ref}_{EPI-Ecl}$ (%) | $-1 < \chi < 1$ (%) | $\overline{\Delta D}_{EPI-Ecl}$ (%) |
| 1 | 03/02/2006 | - | - | - | - |
| 2 | 05/05/2006 | - | - | - | - |
| 3 | 05/19/2006 | - | - | - | - |
| 4 | 05/25/2006 | - | - | - | - |
| 5 | 06/13/2006 | - | - | - | - |
| 6 | 06/19/2006 | - | - | - | - |
| 7 | 11/09/2006 | Fail | -0.5 | 89.3 | -1.3 |
| 8 | 05/02/2007 | - | - | - | - |
| 9 | 05/09/2007 | Pass | -1.9 | 93.8 | -1.2 |
| 10 | 11/07/2007 | Pass | 0.7 | 96.6 | 0.7 |
| 11 | 02/26/2008 | Pass | -0.2 | 98.3 | -0.8 |
| 12 | 02/29/2008 | Pass | -0.4 | 96.5 | -0.8 |
| 13 | 05/22/2008 | - | - | - | - |
| 14 | 6/19/2008 | Pass | -0.5 | 95.8 | -0.7 |
| 15 | 08/07/2008 | Pass | -0.5 | 95.3 | -0.9 |
| 16 | 08/07/2008 | Pass | -0.3 | 94.4 | -0.6 |
| 17 | 09/25/2008 | Fail | -1.7 | 84.6 | -1.9 |
| 18 | 10/06/2008 | Fail | -2.3 | 80.6 | -1.8 |
| 19 | 10/31/2008 | Fail | -3.7 | 99.1 | -0.9 |
| 20 | 01/29/2009 | Fail | -2.1 | 88.0 | -1.8 |
| 21 | 01/30/2009 | Pass | -0.4 | 99.4 | -0.7 |
| 22 | 03/05/2009 | Pass | -0.5 | 98.5 | 0.0 |
| 23 | 03/16/2009 | Fail | -3.1 | 88.5 | -1.9 |
| 24 | 04/02/2009 | Pass | -1.0 | 99.3 | -0.8 |
| 25 | 06/15/2009 | Fail | -3.2 | 94.8 | -0.6 |
| 26 | 06/15/2009 | Fail | -3.9 | 81.8 | -1.6 |
| 27 | 06/17/2009 | Fail | -2.5 | 85.3 | -1.7 |
| 28 | 07/14/2009 | Fail | -1.7 | 87.8 | -2.0 |
| 29 | 08/24/2009 | - | - | - | - |
| 30 | 10/02/2009 | Fail | -2.3 | 80.9 | -1.7 |

current method of pixel-by-pixel dark field subtraction was not implemented until mid August of 2008, which, in light of the fact that the EPID of the primary linac had been malfunctioning for an unknown amount of time, could have significantly impacted the results for plans 10, 12-16. Even with the implementation of a dark current pixel-by-pixel correction, dark current was still problematic until the EPID was repaired (June of 2009). For these reasons, it was presumed that EPID malfunction was a contributing factor for the clinical failure of 21, 22, and 24, measured before the EPID cassette was replaced. High mean dark current pixel values were observed for these three plans indicating that EPID malfunction had likely occurred at the time of measurement. Second, two of those clinical failures were identified using the secondary linac (plans 9 and 11), and were therefore subject to systematic differences in outcome.

The discrepancy in EPID dark current could have contributed to some verification plans being falsely identified as passes, whereas they would have been considered failures if they had been measured under more stable conditions. With this consideration, it was possible that the failures identified as consistent, identified in Table 4.2, only formed a subset of true verification failures. In any case, roughly 50% (11) of the 21 redelivered plans were found to fail consistently. Two of those plans failed solely as a result of a discrepancy in reference dose being greater than 3%. The 9 other verifications failed with respect to the percentage of voxels within tolerance ($\chi$ distribution), or a combination of exceeding the action levels for both of these metrics. Concerning all consistent outcomes, no plans failed on the grounds of mean dose difference surpassing the 2% action level[4], and all 21 plans passed the verification criteria for the low dose region of the dose distribution. An explanation for the consistent failure of 11 verifications required further evaluation.

## 4.2 Comparisons to ion chamber measurements

### 4.2.1 Analysis on the basis of plans

Ion chamber point dose measurements for verification failures required that the phantom's centre be at a high dose, low dose gradient location. The generation of a planned dose distribution that met this criteria was attempted for all 11 consistent verification failures (identified in Table 4.2). In 3 instances, re-planning was unsuccessful in meeting the dose criteria, limited in part by the fact that the dose distributions could not be recalculated using the original pencil beam convolution of Eclipse (version 8.1.18) as of late October, 2009, when the TPS was upgraded. This was unfortunate and demonstrated one practical limitation to conducting research in a clinical setting. For the purpose of analysis, the 8 successfully re-planned failures were divided into 2 subgroups: the 6 that had failed in terms of $\chi$ distribution, and

[4]Plan 28 failed in terms of mean dose difference when the 0.1% standard deviation of the dose reconstruction measurement was considered.

the two others that had failed only at the clinical reference point.

Sources of ion chamber measurement uncertainty ($\sigma_{ion}$) were identified in terms of the uncertainty associated with incorrect positioning of the phantom ($\sigma_{pos}$), and the random fluctuations in linac output and ion chamber response ($\sigma_{random}$). $\sigma_{pos}$ was directly related to the positional accuracy of the treatment couch. If a 1 mm shift in ion chamber position was assumed to have occurred in all three orthogonal directions, resulting in a displacement of $\sqrt{3}$ mm, the planned dose distribution requirement of 1% in $\pm$3 mm would have roughly indicated a change in dose of approximately 0.3% at the location of measurement. Gantry sag and defects in the phantom also contributed to phantom positioning uncertainty, assessed at 1 mm for the purposes of analysis. Combining the sources of $\sigma_{pos}$, the uncertainty in dose measurement related to position was assessed to be approximately 0.6%. $\sigma_{random}$ was evaluated as the standard deviation in a series of ion chamber measurements for single open fields (100 MU, X=10 cm, Y=10 cm) and was found to be negligible at 0.05%. Based on these results, $\sigma_{ion}$ was assigned a value of 0.6% and was considered to be a rough estimate of the combined uncertainty associated with all ion chamber measurements.

In Figure 4.7, planned and reconstructed point dose differences with respect to the measured ion chamber dose are plotted for all 8 re-planned failures. The error bars in Figure 4.7 represent the ion chamber measurement uncertainty, added in quadrature with the 0.4% standard deviation of the dose reconstruction measurements for the relevant data points. One important observation was that the dose measured with the ion chamber was in agreement with the planned dose, or between the planned and reconstructed point doses. This indicated that all planned and reconstructed doses were not grossly erroneous.

Concerning the plans that had originally failed in terms of the chi distribution, the mean difference between planned and reconstructed dose at the point of ion chamber measurement was $-2.7 \pm 0.3\%$ ($\mu \pm \sigma$). Collectively, relative to the ion chamber

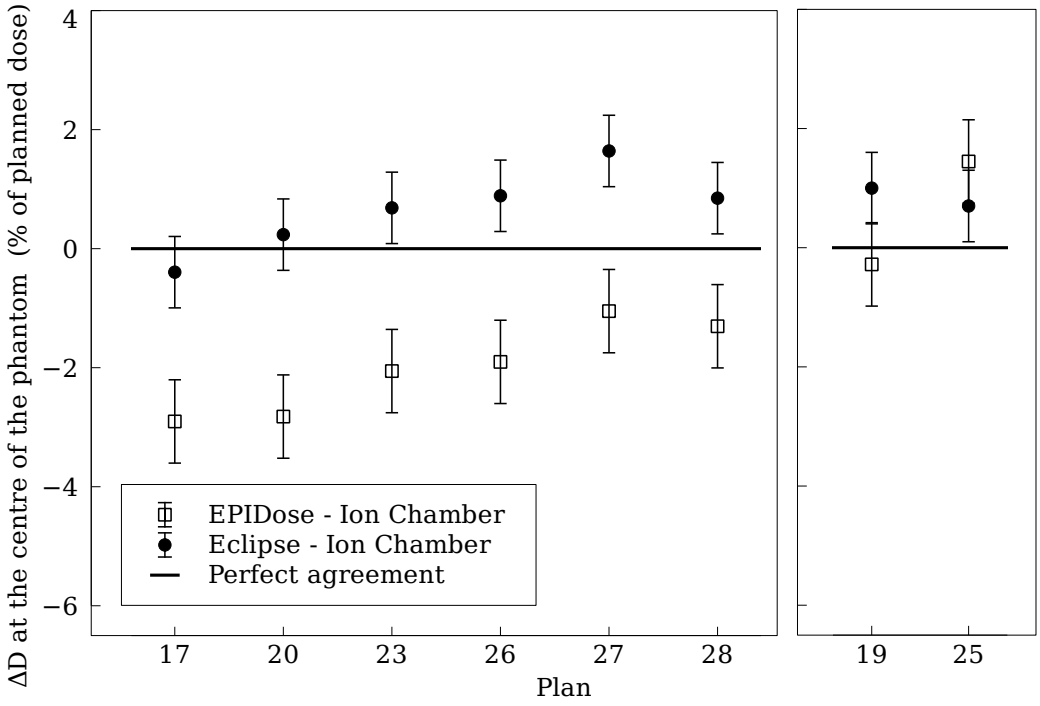


**Figure 4.7:** Planned and EPIDose reconstructed point dose differences with respect to ion chamber dose measurements, as a percentage of planned dose, for the re-planned dose distributions of 8 consistent verification failures. The plans that had only failed at the reference point are separated from the other plans (right side of figure). Point dose comparisons were limited to the centre of the phantom, which was a location of high dose with a low dose gradient, and thereby representative of a clinically acceptable reference point.

measurements, planned dose calculations were observed to overestimate the dose by $0.7\% \pm 0.7\%$ ($p < 0.03$; paired t-test[5], 1-tailed), where as EPIDose underestimated the dose by $-2.0 \pm 0.8\%$ ($p \ll 0.01$). In the majority of instances (4 of 6), the discrepancies in $\Delta D_{EPI-Ecl}$ were the result of combined contributions from both the dose calculation and the EPIDose dose reconstruction. The standard deviation of $\Delta D_{EPI-Ecl}$ was observed to be less than half of that for $\Delta D_{EPI-Ion}$ or $\Delta D_{Ecl-Ion}$. This was representative of the fact that there was error in each ion chamber measurement which was equally attributed to both $\Delta D_{EPI-Ion}$ and $\Delta D_{Ecl-Ion}$. The discrepancies in point doses ($\Delta D_{EPI-Ecl}$) evaluated for plans 19 and 25 were -1.2% and 0.8%, respectively, and were not considered resolvable. These plans were unlikely candidates to produce meaningful discrepancies for alternative points because they had already shown to agree for an acceptable percentage ($> 90\%$) of high dose voxels.

On the basis of single point dose measurements, these results indicated that inaccuracy in the EPIDose measurement was the greatest contributing factor to the verification dose discrepancies. However, none of the dose discrepancies had exceeded the clinical reference dose action level (3%) and were, for that reason, not necessarily representative of clinical failure measurements. Moreover, the majority of consistent failures had failed as a result of volumetric discrepancies ($\chi$ distribution), for which the above analysis of point doses may not be applicable. Additional sources of ion chamber measurement uncertainty included the effects of averaging the dose measurements over the volume of the ion chamber, as well as, perturbation to the dose distribution resulting from the presence of the dosimeter. These contributions to error were not quantified but were considered to limit the utility of ion chamber measurements for resolving the source of dose discrepancies between $D_{EPI}$ and $D_{Ecl}$.

[5]Hypothesis testing was designated a significance level of $\alpha = 0.05$

### 4.2.2 Analysis on a field-by-field basis

Ion chamber measurements were evaluated on the basis of individual fields. The purpose of this analysis was to investigate how the contributing fields of each plan had combined to create the observed dose discrepancies. By design, the analysis was limited to those plans for which resolvable discrepancies between planned and reconstructed point doses had been identified, plans 17, 20, 23, 26, 27, and 28. Combined, this provided 56 individual dose measurements originating from 6 plans, again, producing an average point dose discrepancy of $-2.7 \pm 0.3\%$. Given the ion chamber positioning uncertainty relative to the modulated IMRT fields, measurement uncertainties could have only been estimated with low precision The analysis was therefore restricted to uncovering gross trends in the data and comparing those trends to the inherent variability.

For each of the 56 fields, the planned and EPIDose reconstructed dose measurements were made relative to the corresponding ion chamber measurement and recorded as a percentage of the planned reference dose. The resulting distributions are provided as histograms in Figure 4.8. These distributions were found to be significantly different ($p \ll 0.01$; paired t-test, 1-tailed). Only 2 fields were shown to produce dose discrepancies above 1%. Fields delivering less than 1 cGy (planned) were not found to contribute significantly to the dose discrepancies, where each field had resulted in a dose difference of less than 0.1%. In searching for problematic fields, each plan was evaluated individually. The largest value for $|\Delta D_{EPI-Ecl}|$ was found to be 1.2%, and for 5 of the 6 plans, the largest discrepancy was below 1%. This indicated that the discrepancies of the 6 plans were not simply the result of 6 problematic fields and were more appropriately described by the accumulation of errors originating from the offset in the distributions of planned and reconstructed doses.

Reconstructed and planned doses for the subset of individual fields with point

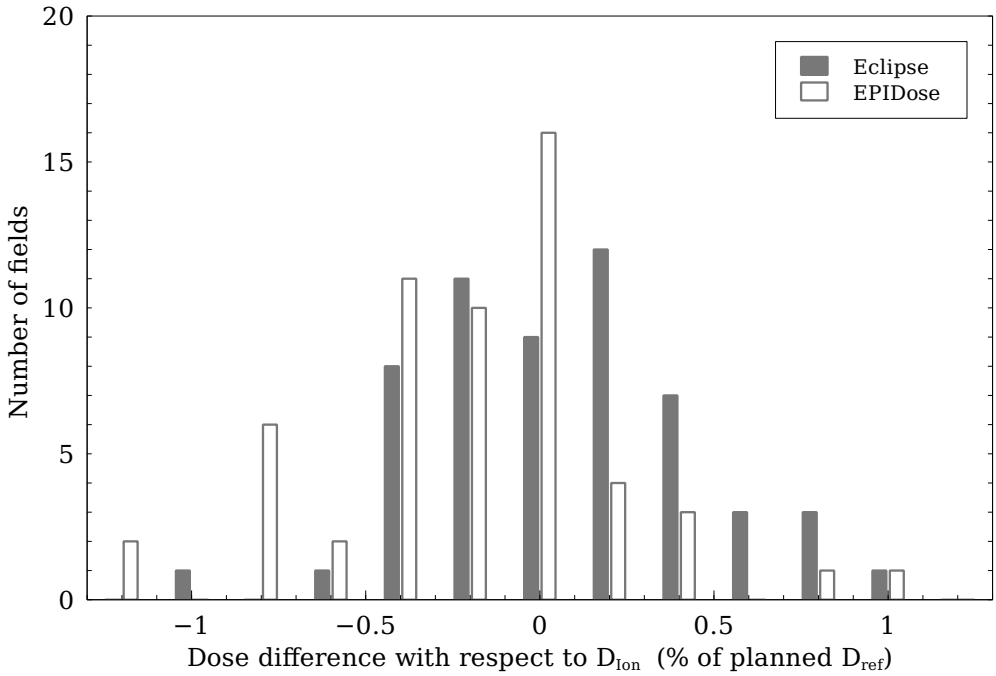


**Figure 4.8:** The distribution of dose differences on the basis of individual fields with respect to ion chamber dose measurements (% of total dose of the plan). Histograms were constructed with 0.2% bin width, and 56 IMRT fields were evaluated individually.

doses above 10 cGy were plotted as a function of the dose measured with an ion chamber, shown in Figure 4.9. Doses below 10 cGy were not considered because of an expected nonlinear dose response from the EPID with respect to energy, relevant for low dose measurements which have a relatively higher proportion of scatter, for which the high atomic number of gadolinium produces a disproportionate response. Linear fits were performed for each data set, and the fit results are summarized in Table 4.3. The 0.08 cGy offset between the two linear fits was considered insignificant to the verification discrepancies. The different proportionality constants of the two linear fits suggested that discrepancies between $D_{EPI}$ and $D_{Ecl}$ were proportional to dose. $\Delta D_{EPI-Ecl}$ is plotted against $D_{Ion}$ in Figure 4.10. The significance of the potential dose dependence for $(\Delta D_{EPI-Ecl})$ was evaluated in terms of correlation. The linear correlation coefficient (r) was calculated for the two variables (labeled

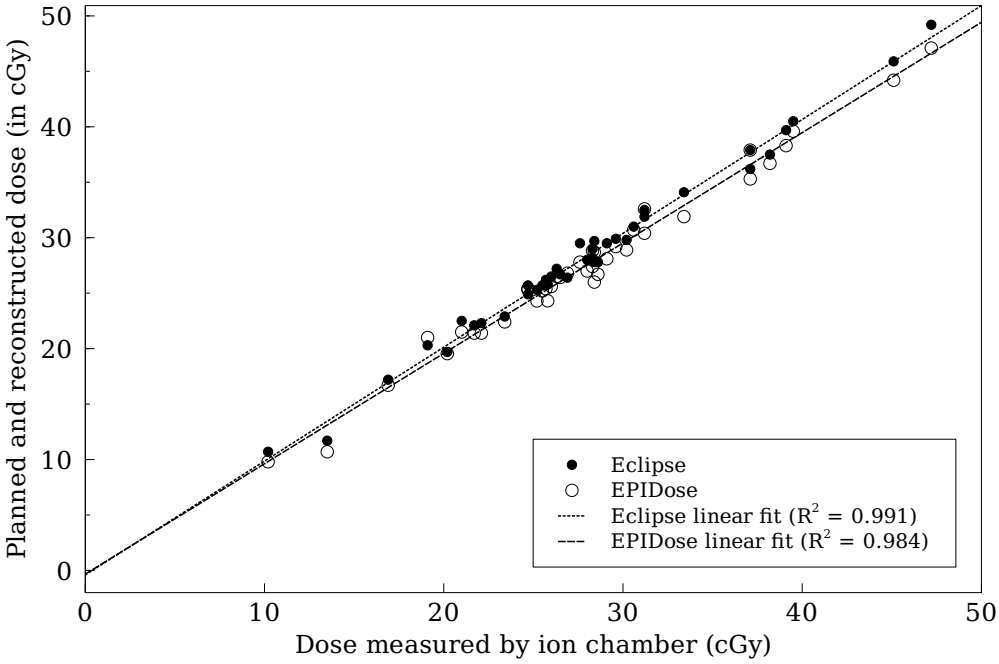


**Figure 4.9:** Planned and EPIDose reconstructed point doses as a function of dose measured with an ion chamber, for 40 individual fields above 10 cGy.

**Table 4.3:** Using the method of least squares, the individual field data for calculated $D_{Ecl}$ and reconstructed point doses $D_{EPI}$ was fit linearly as a function of ion chamber dose.

| | Linear fit (in cGy) | $R^2$ |
|---|---|---|
| Planned (TPS) | $D_{Ecl} = 1.0266(D_{Ion}) - 0.4018$ | 0.984 |
| EPIDose dose reconstruction | $D_{EPI} = 0.9951(D_{Ion}) - 0.3286$ | 0.991 |

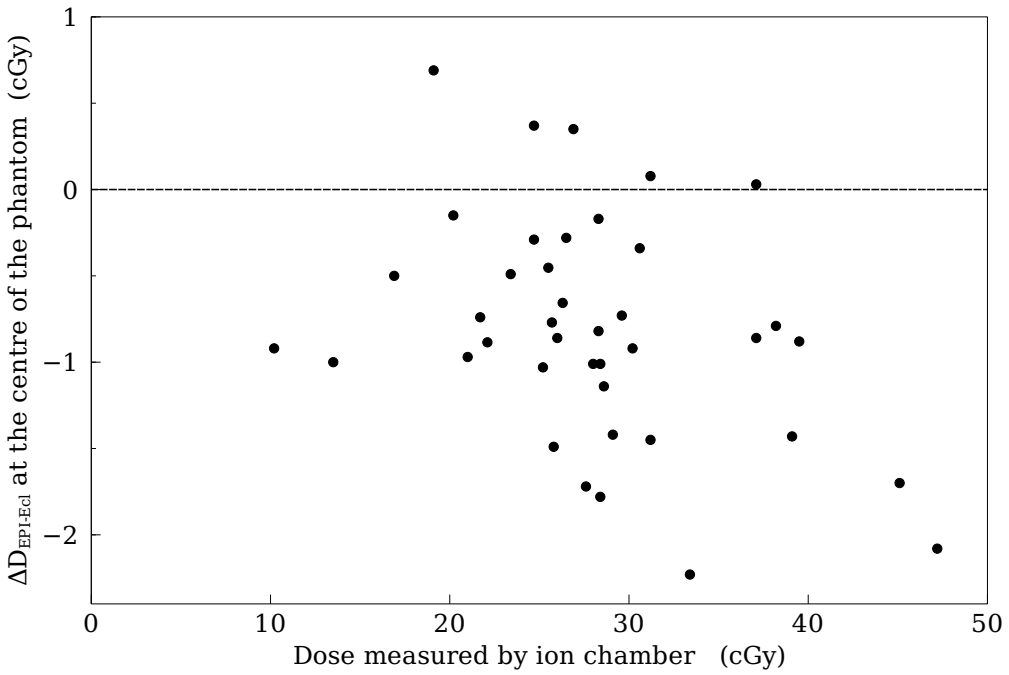


**Figure 4.10:** Point dose differences (EPIDose-Eclipse) plotted against ion chamber measured dose for the 40 individual fields planned above 10 cGy. These variables were shown to be independent, demonstrating an insignificant correlation, r = -0.37 ($p < 0.06$).

here as $x$ and $y$) using Equation 4.1 [51]:

$$r = \frac{\sum(x_i - \bar{x})(y_i - \bar{y})}{[\sum(x_i - \bar{x})^2 \sum(y_i - \bar{y})^2]^{1/2}} \tag{4.1}$$

The significance of calculating the value of r for a given data set was assessed in terms of the probability $p$ for which N measurements would have produced a value of $r$ greater than or equal to the calculated correlation coefficient when no correlation existed. This probability distribution has been calculated [51]. The linear coefficient of correlation (r) between $\Delta D_{EPI-Ecl}$ and $D_{Ion}$ was greater than -0.37 ($p < 0.06$). Based on these results, the correlation between verification dose discrepancies and dose was considered weak, if not insignificant. This indicated that the development of verification discrepancies was not dose dependent (within the uncertainties of measurement) and more complicated in origin.

# Chapter 5

# Results and Discussion II: Impact of advanced dose calculation engines and plan complexity on verification metrics

The planned dose distributions of all consistent verification failures were recalculated using AAA and Monte Carlo (MC). In general, verification outcomes improved using the advanced dose calculation engines, compared to the PBC. Fluence modulation was shown to be correlated to the outcomes of verification, where the aperture geometry-based quantity $\overline{r_X}$ was shown to be more correlated then either average leaf gap or the modulation index. The superior capabilities of the advanced dose calculations in regards to MLC modeling and fluence transport were believed to be responsible for the improvements in verification outcomes.

## 5.1 Alternative dose calculations for failures

### 5.1.1 Evaluation of verification metric uncertainty

The uncertainties summarized in Table 4.1 were attributed to the verification metrics of all 11 consistent failures. In doing so, the standard deviation in reference dose differences ($\sigma_{\Delta D_{ref}}$) and mean dose differences ($\sigma_{\overline{\Delta D}}$) between EPIDose and Eclipse were assumed to equal 0.4% and 0.1%, respectively. These uncertainties were related

to the statistical uncertainty of EPI measurements, not the planning dose calculation algorithm and were directly attributed to the verification metrics determined using AAA. For the comparisons made between EPIDose reconstructed dose distributions and Monte Carlo, the statistical uncertainty in $\overline{\Delta D}_{EPI-MC}$ was not known. Using the fact that the MC calculations had requested approximately the same uncertainty in point dose as the standard deviation in EPIDose reference point dose measurements (0.5%), these contributions were assumed to be equal for all high dose region voxels. In this way, the contributions to to dose uncertainty from EPI measurements and MC were considered to be equal and added in quadrature before being attributed to $\overline{\Delta D}_{EPI-MC}$.

The majority of consistent verification failures were determined on the basis of chi distribution. The reproducibility measurements summarized in Section 4.1.3 revealed that the statistical uncertainty in these distributions was related to the percentage of voxels within tolerance ($V_{|\chi|<1}$). This was expected and explained in the following way: As $V_{|\chi|<1}$ decreased, a greater proportion of the voxels bordered the tolerance values. A small variability in the dose of a large number of voxels bordering the tolerance values would translate to a large value of $\sigma_\chi$. For this reason, the variability in chi-distribution was linearly interpolated/extrapolated from known values of the two plans in Table 4.1. A unique value of $\sigma_\chi$ was calculated for each plan, and was proportional to the percentage of voxels within tolerance (Equation 5.1):

$$\sigma_\chi = 20.7 - 0.2V_{|\chi|<1}\ (\%) \tag{5.1}$$

This was considered to provide the best available estimate of $\sigma_\chi$ for each consistent failure, and attributed equally to $\chi$ distributions derived from the PBC and AAA. For reasons described above, this uncertainty in $\chi$ distribution was multiplied by $\sqrt{2}$ for comparisons between EPIDose reconstructed and MC calculated dose distributions.

### 5.1.2 Verification outcomes using AAA and MC

For each consistent failure, the EPIDose reconstructed dose distribution was compared to dose distributions calculated using the PBC, AAA, and MC. In one instance (plan 27), the MC dose calculation was not successfully accomplished, for which neither the cause nor a resolution was identified. Figure 5.1 shows the results in terms of the percentage of voxels within tolerance. Error bars indicate the uncertainty in each result, discussed in Section 5.1.1. For the purposes of analysis, the 11 plans were divided into two subgroups: the nine plans that had failed in terms of the $\chi$ distribution, and the remaining two that had not. All of the verification plans that

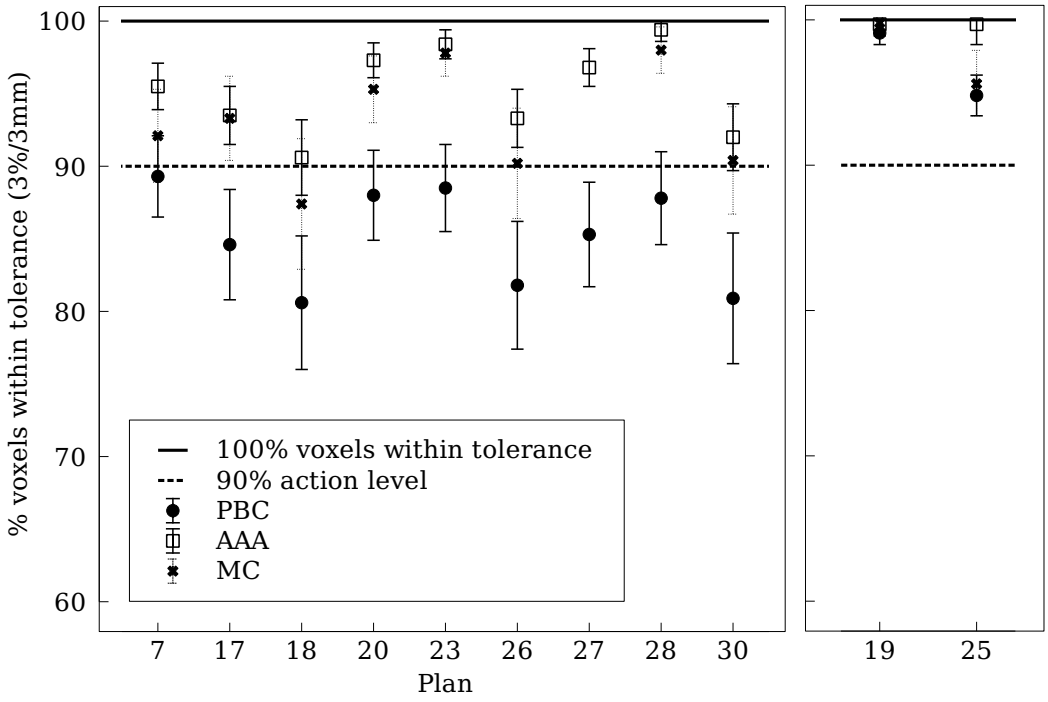


**Figure 5.1:** The percentage of voxels within tolerance with respect to planned dose calculated with the PBC algorithm, and two superior calculation engines: AAA and MC. Error bars represent the standard deviation assumed from the above reproducibility experiments, and the statistical uncertainty in voxel dose of the MC calculations.

had consistently failed were shown to pass when the PBC was replaced with AAA. The AAA dose calculations were confirmed by MC, although the uncertainty in the MC dose calculations was greater than for AAA and in some cases (plans 7 and 18)

MC overlapped the results of both algorithms.

Reference dose differences resulting from each dose calculation engine are shown in Figure 5.2, where again, two subgroups have been identified in accordance with the 3% action level. All 4 failures of the $\Delta D_{ref}$ verification criteria were shown to

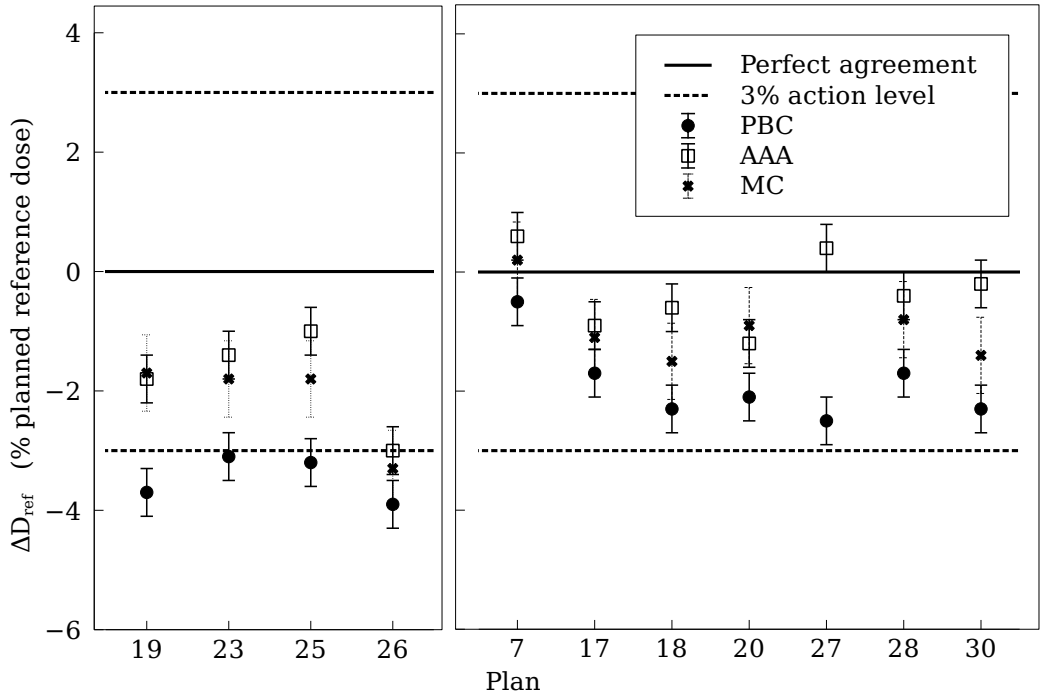


**Figure 5.2:** Reference dose difference ($\Delta D_{ref}$) for each consistent verification failure, determined using the PBC, AAA, and MC. Error bars represent the 0.4% standard deviation in EPIDose measurements (added in quadrature with the 0.5% uncertainty of the MC calculations for the respective MC-based dose differences).

pass using AAA. These results were confirmed by MC, with the exception of plan 26, where the improvement in $\Delta D_{ref}$ was not considered significant with consideration to the point dose uncertainty. Verification outcomes in terms of $\Delta D_{ref}$ improved in general for all consistent failures.

The effect of dose calculation engine on $\overline{\Delta D}$ is shown in Figure 5.3. Although none of the consistent failures had mean dose differences that surpassed the action level (2%), $\overline{\Delta D}$ improved for these plans, in general. Verification outcomes concerning each dose calculation engine are summarized in Table 5.1, in terms of mean and

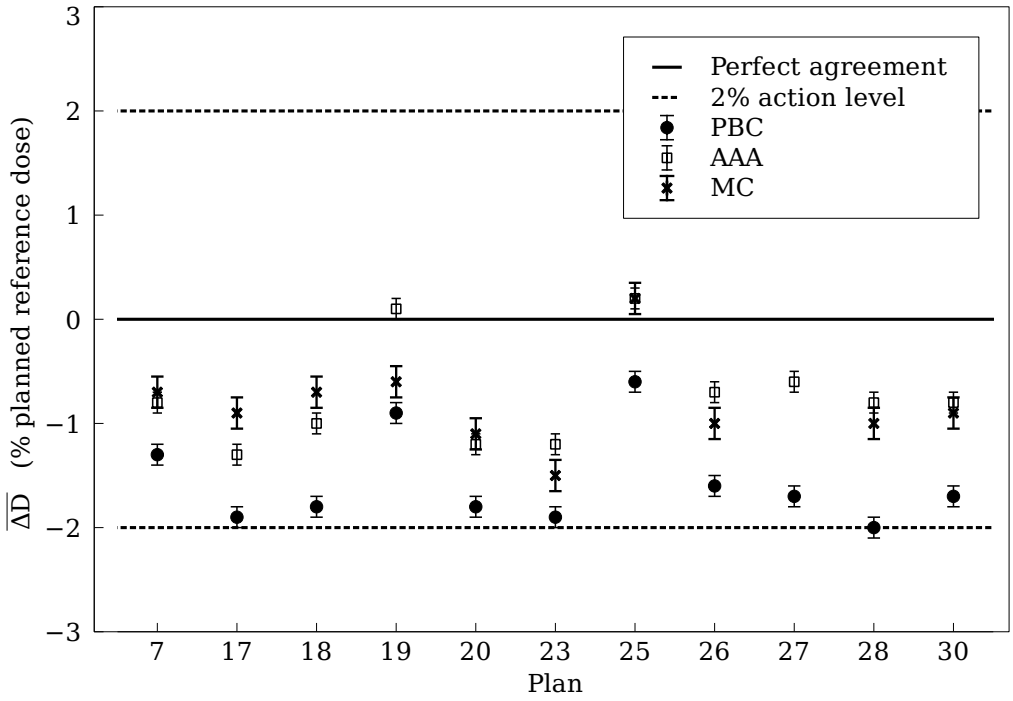


**Figure 5.3:** The mean dose differences ($\overline{\Delta D}$) between EPIDose reconstructed dose and calculated dose (using PBC, AAA and MC) for each consistently failing verification plan.

standard deviation.

## 5.2 Evaluation of plan complexity

High fluence modulation was believed to be a contributing factor to the development of discrepancies between the planned and EPIDose reconstructed dose distributions of IMRT verification plans. Discovering a relation between fluence modulation and verification outcome would suggest possible mechanisms by which verification failures could have been produced, and thereby indicate possible methods of resolving future verification failures. In order to assess the impact of fluence modulation on the verification process, verification plans were evaluated for three quantities: the average leaf pair gap (the average separation of MLC leaf pairs), the average modulation index (MI) (see Section 3.3.1), and the average AP-ratio ($\overline{r_X}$) (see Section 3.3.2). Since the majority of verification failures had failed as a result of having less than 90% of high dose region voxels within tolerance, the outcomes of verification were described

**Table 5.1:** A summary of the verification outcomes of consistent failures using three different calculated dose distributions: The PBC, AAA, and Monte Carlo. Results are reported for the subgroup of plans that had consistently failed in terms of the specific verification metric, as well as, for all plans combined. $n$ refers to the number of plans for which the mean and standard deviation are calculated. Verification metrics were only evaluated for the high dose region (voxels with dose above 80% of the planned reference dose).

| Verification metric | Plans ($n$) | PBC | AAA | MC |
|---|---|---|---|---|
| Voxels within tolerance (%) | Failures (9) | 85.2±3.4 | 95.2±3.0 | 93.1±3.8 ($n = 8$) |
| | All (11) | 87.3±5.7 | 95.7±3.0 | 94.0±4.0 ($n = 10$) |
| Reference dose difference (%) | Failures (4) | -3.5±0.4 | -1.8±0.9 | -2.1±0.8 ($n = 4$) |
| | All (11) | -2.5±1.0 | -0.9±1.0 | -1.4±0.9 ($n = 10$) |
| Mean dose difference (%) | All (11) | -1.6±0.4 | -0.7±0.5 | -0.8±0.4 ($n = 10$) |

in terms of $V_{|\chi|<1}$ for the purposes of correlation analysis. Fluence modulation was quantified for ten additional verification plans that had been shown to consistently pass the verification criteria. In this way, the relationship between fluence modulation and verification outcome was explored for a set of outcomes that spanned the action level.

### 5.2.1 MLC leaf separation analysis

The average distance separating MLC leaf pairs during the delivery of an IMRT field was related to the fluence modulation in the following way: the dMLC IMRT fields were delivered as dynamic sliding windows, with a maximum dose rate of 400 MU/min. During planning stages, the MLC leaf motion calculator of Eclipse was used to determine the motion of MLC leaf pairs that was required to produce the optimal fluence. Given the limit on dose rate and the required intensity variations, the TPS minimized the required number of MU by creating an MLC leaf sequence that maximized the required leaf gaps. As the fluence modulation increased, the

space between MLC leaf pairs was required to decrease. In this way, the average leaf gap of an MLC plan was considered a simple means of quantifying the average relative fluence modulation of the plan.

In Figure 5.4, plan averaged MLC leaf gaps are plotted against the percentage of voxels within tolerance for 21 IMRT verification plans. In general, the plans that had

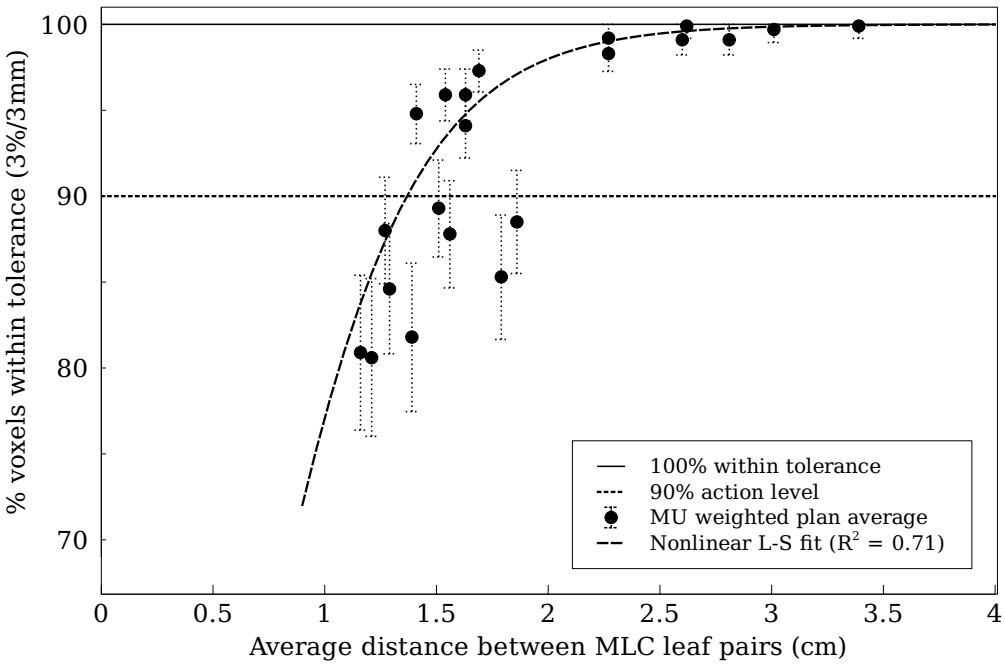


**Figure 5.4:** The percentage of voxels within tolerance ($V_{|\chi|<1}$) plotted with respect to the average MLC leaf separation, for 21 verification plans. The relationship between $V_{|\chi|<1}$ and average leaf-gap was assumed to be sigmoidal and fit using a logistic function.

average leaf gaps greater than 2.3 cm had over 98% of voxels within tolerance upon verification. This is in contrast to those plans with smaller average leaf gaps, where the verification outcomes were more variable. The relationship between $V_{|\chi|<1}$ and average leaf-gap was assumed to be sigmoidal. For this reason, the data was fit with a logistic function using the weighted[1] nonlinear least squares method. The result of the fitting operation is also shown in Figure 5.4.

In order to quantify the correlation between $V_{|\chi|<1}$ and average leaf-gap, a log

[1]Each data point was weighted by the inverse of the variance, $1/\sigma^2$.

transform (equivalent to the inverse of the fitted logistic function) was applied to $V_{|\chi|<1}$. The transformed data is plotted against average leaf gap in Figure 5.5. By

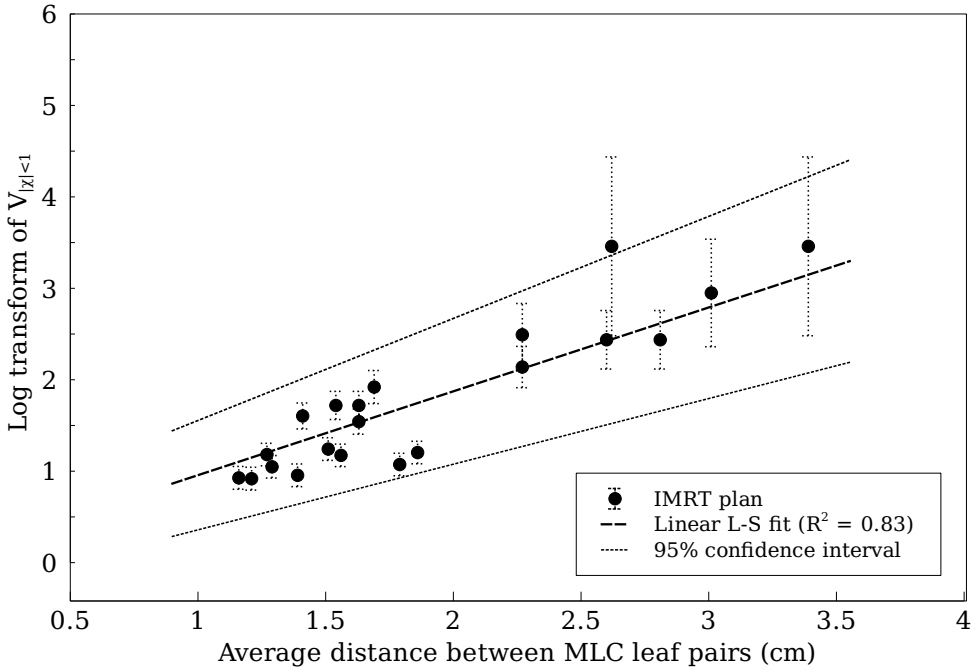


**Figure 5.5:** The log transform of $V_{|\chi|<1}$ plotted with respect to average leaf separation ($r = 0.91$, $p \ll 0.01$).

applying Equation 4.1 to these two quantities, the linear correlation coefficient (r) was found to be 0.91 ($p \ll 0.01$). These results demonstrated that fluence modulation was significantly correlated with the production of verification failures. Although the correlation was highly significant, average leaf separation was considered limited in its ability to discriminate against poor verification outcomes due to the high level of variability in verification outcome with respect to leaf separations ranging between 1.3-2.0 cm.

### 5.2.2 Modulation index analysis

The fluence modulation of the 21 verification plans was also quantified in terms of the modulation index (see Section 3.3.1). As an example of this calculation, Figure 5.6 shows the spectra calculated for a seven field plan. The spectra represented the

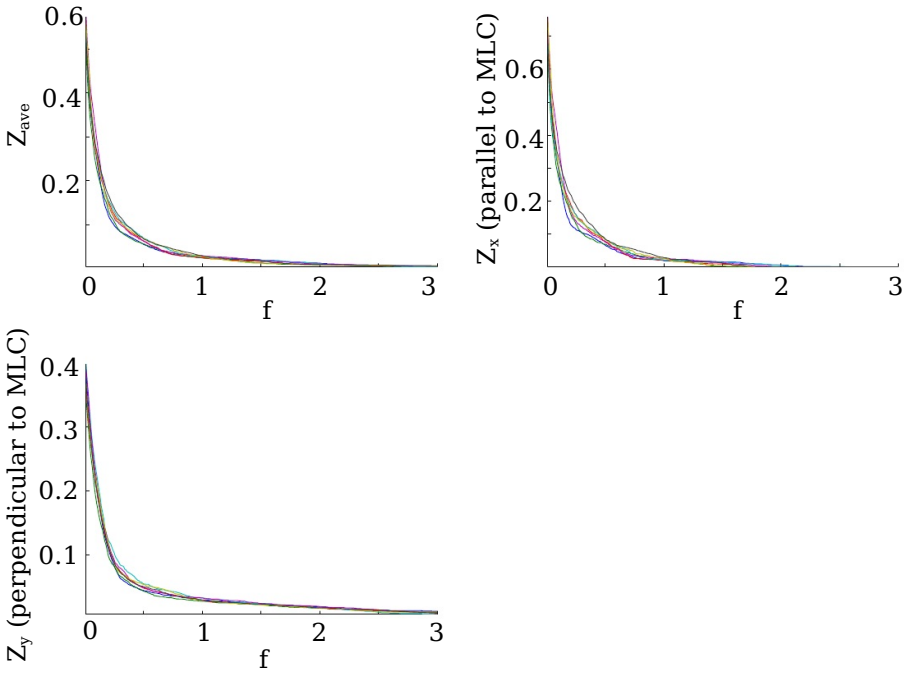


**Figure 5.6:** The spectra ($Z$) calculated for a seven field IMRT verification plan, provided as an example. Each field is identified with an individual colour. $f$ is a fraction of the standard deviation.

relative amount of variation in the fluence above a certain fraction (f) of the standard deviation. The directional components of each spectrum was evaluated individually (also shown in Figure 5.6). Spectra were integrated to an upper integration limit, $F$, ranging between 0.01 and 3.00 to produce the modulation indices of the fields as a function of F (shown in Figure 5.7). For the purposes of analysis, the modulation index of each field was evaluated as a single value for F=3, although no optimization of this value was attempted.

An MU weighted average value for MI(F=3), was calculated for each of 21 verification plans. This provided a single value for each plan that was then compared to the respective verification outcomes. The values of $\mathrm{MI}_{ave}$ are plotted with respect to the percentage of voxels within tolerance in Figure 5.8. Based on these results, no significant correlation between $\mathrm{MI}_{ave}$ and verification outcome was found.

The same analysis was repeated for $\mathrm{MI}_x$ and $\mathrm{MI}_y$, and the results are shown in

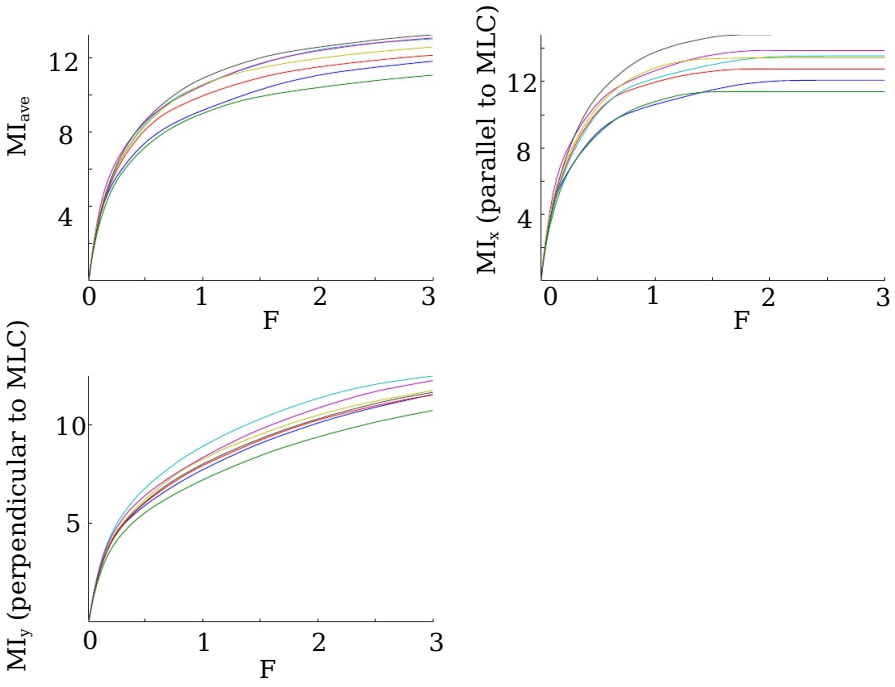


**Figure 5.7:** The modulation indices calculated for the spectra presented in Figure 5.6, with respect to the upper integration limit, $F$.

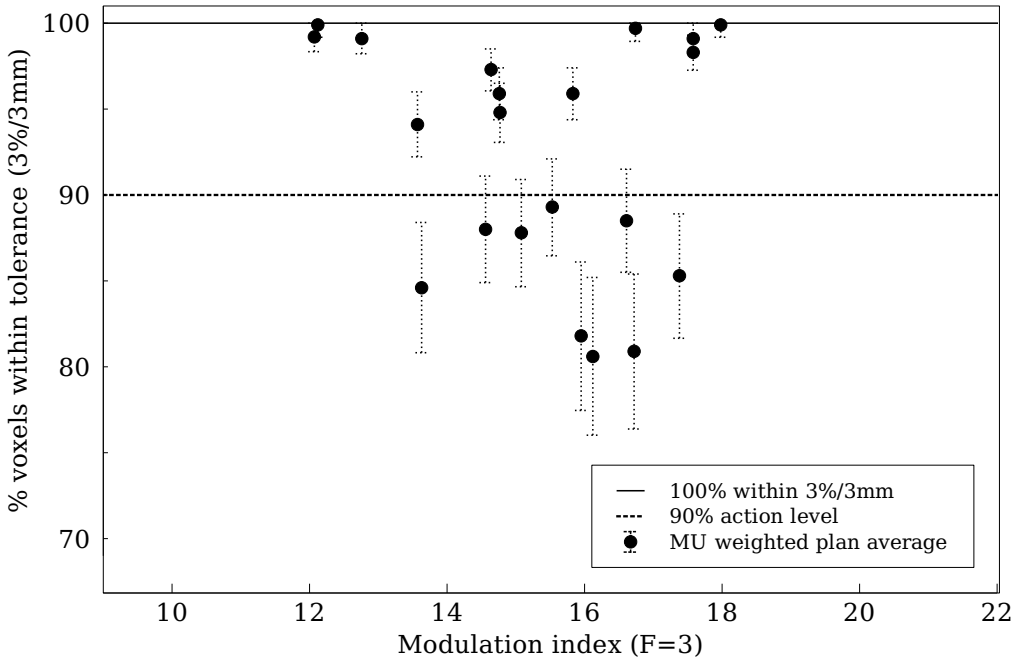


**Figure 5.8:** The percentage of voxels within tolerance plotted against the modulation index ($\mathrm{MI}_{ave}$). These quantites were not found to be correlated.

Figure 5.9. In an identical fashion to the analysis of average leaf gap, a sigmoid function was fit for $MI_x$ (see Figure 5.9a). A significant correlation between the $MI_x$ and the log transform of $V_{|\chi|<1}$ was found (r=-0.75, $p < 0.001$). No significant correlation was found with respect to $V_{|\chi|<1}$ and $MI_y$. This indicated that, in averaging the spectral components, calculating $MI_{ave}$ had resulted in a significant loss of information, namely, the significant correlation in fluence modulation parallel to the direction of MLC motion ($MI_x$).

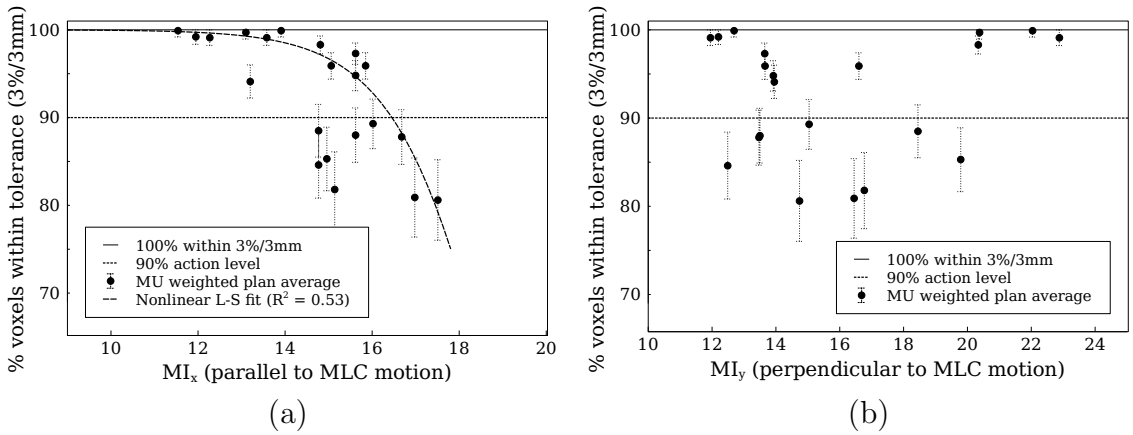


**Figure 5.9:** The modulation indices, **(a)** $MI_x$ and **(b)** $MI_y$, corresponding to fluences evaluated in directions parallel and perpendicular to MLC motion, respectively. In the case of $MI_x$, the data was assumed to be sigmoidal and fit with a logistic function.

### 5.2.3 Aperture area-perimeter ratio analysis

The mean AP-ratio ($\overline{r_X}$), defined in Section 3.3.2, was used to quantify plan complexity with respect to MLC aperture geometry. The $\overline{r_X}$ was calculated for each of the 21 IMRT verification plans. Figure 5.10 provides the aperture area, perimeter and associated ratio with each MLC aperture (defined for the complete series of control points) for a 7 field verification plan. After generating these quantities for each plan, Equation 3.2 was used to calculate $r_X$. A single quantity $\overline{r_X}$ was attributed to each verification plan by averaging the $r_X$ of each contributing field, weighted by MU (Equation 3.3).

In Figure 5.11, the percentage of voxels within tolerance associated with each

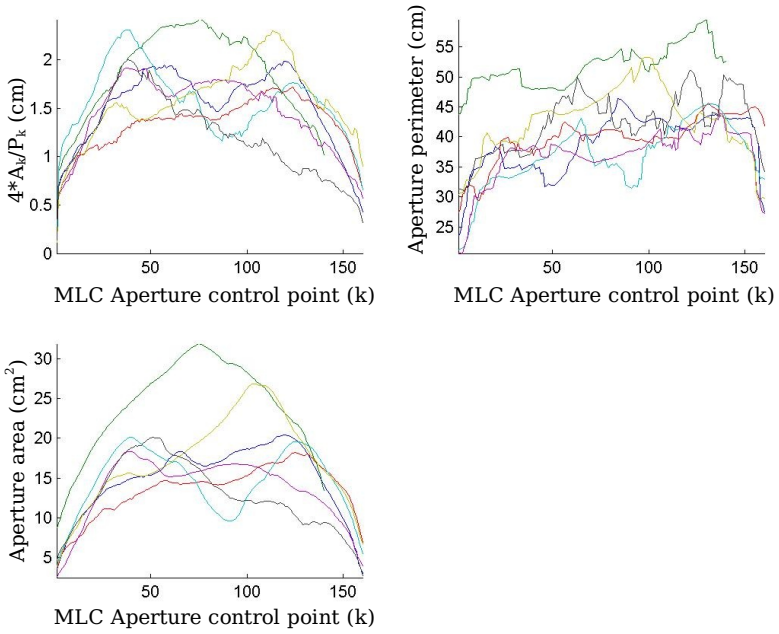


**Figure 5.10:** The quantities associated with calculating $\overline{r_X}$ for a seven field verification plan, provided as an example. Each field is identified with an individual colour.

verification plan is plotted against $\overline{r_X}$. The data was fit using a logistic function and the log transform of $V_{|\chi|<1}$ is plotted with respect to $\overline{r_X}$ in Figure 5.12. The correlation between the log transform of $V_{|\chi|<1}$ and $\overline{r_X}$ was 0.95 ($p \ll 0.01$). Based on these results, $\overline{r_X}$ was considered to better discriminate against problematic IMRT verification plans than either the average leaf-gap, or $MI_x$.

In Figure 5.13, The MU weighted averages for aperture area and perimeter are plotted against $V_{|\chi|<1}$, for which the correlations were not significant. Based on these results, $\overline{r_X}$ was a stronger indicator of verification outcome compared to either mean aperture area or mean aperture perimeter, alone.

### 5.2.4 Discussion of results

In general, the outcomes of IMRT verification failures improved when the PBC-calculated dose distribution was re-calculated using more advanced methods (AAA including a new version of the LMC, or MC). Moreover, all of the consistent fail-

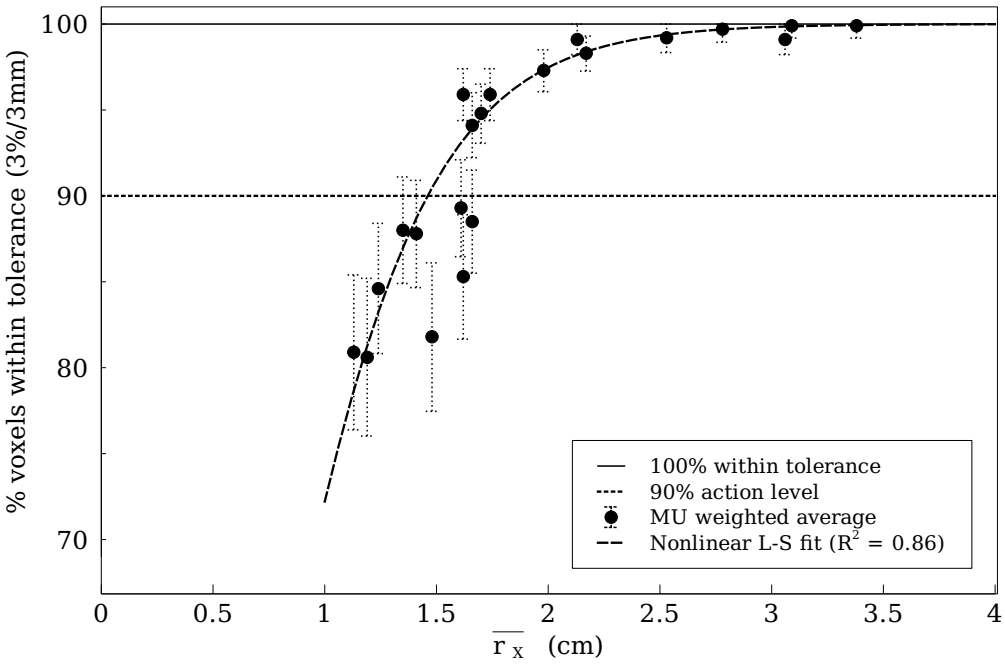


**Figure 5.11:** The percentage of voxels within tolerance plotted with respect to $\overline{r_X}$, for 21 IMRT verification plans.

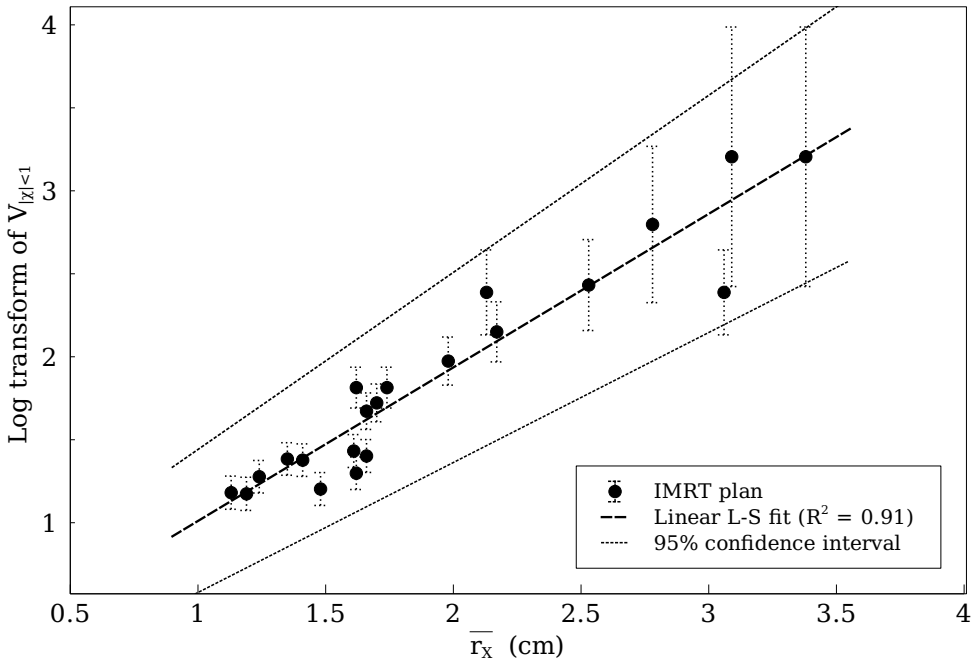


**Figure 5.12:** The log transform of $V_{|\chi|<1}$ plotted with respect to $\overline{r_X}$ ($r = 0.95$, $p \ll 0.01$).

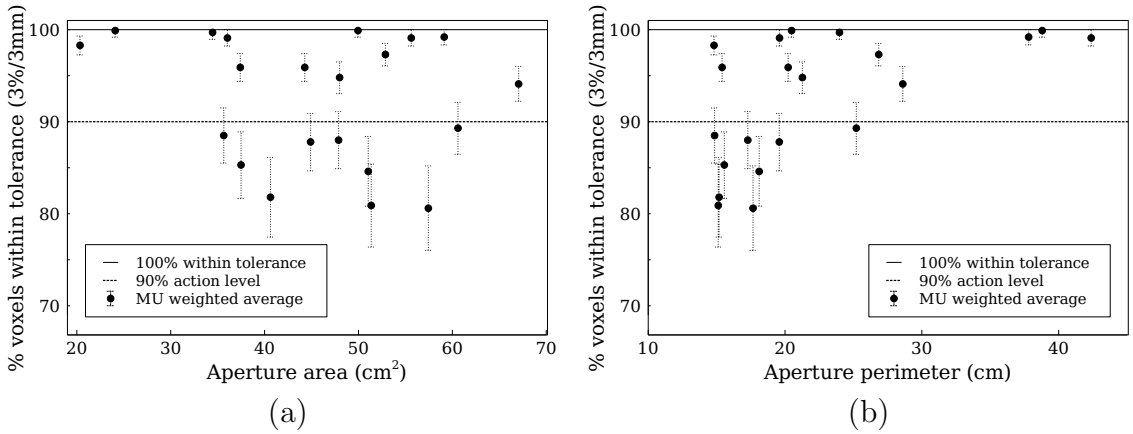


**Figure 5.13: (a)** The average area and **(b)** average perimeter of MLC apertures defined by the MLC positioning sequence (MU weighted) for 21 verification plans, plotted against the outcomes of verification.

ures were shown to pass with respect to each verification metric ($V_{|\chi|<1}$, $\Delta D_{ref}$ and $\overline{\Delta D}$), when the planned dose distribution was calculated with AAA. These alternative dose calculation engines were believed to be more accurate than the PBC, and this demonstrated that deficiencies in the PBC and/or the older version of the LMC were significantly contributing to the development of verification failures. In addition, verification outcomes were shown to worsen significantly with increasing fluence modulation. The evident improvement in dose calculation for highly modulated fluences observed for AAA calculations was possibly attributable to the superior accuracy of two factors generally related to fluence and fluence transport: The upgraded LMC used for AAA calculations, and the superior characterization of photon energy spectra.

As average leaf separation decreased, a greater proportion of the calculated dose was dependent on the accuracy of the DLS. For extremely small separations, DLS may in fact become insufficient in accounting for the rounded MLC leaf tips. The relative impact of the upgraded LMC used for AAA calculations (corresponding to the more accurate calculation of actual fluences) was not evaluated independently of the algorithm. An alternate set of PBC dose calculations using the upgraded software

(Eclipse version 8.6.15) would have been useful in discriminating between dose differences attributable to the algorithm or version of the LMC. Regardless, AAA IMRT verification planning was clinically implemented in March 2010. The extra-focal photon source of AAA allowed for a higher accuracy in calculating dose penumbra (see Section 2.5), and this could be extended to dose gradients, in general. In this way, the intensity modulation of IMRT fields could have translated proportionately to differences in AAA and PBC dose distributions.

Compared to average leaf separation and $MI_x$, $\overline{r_X}$ was considered to be a better discriminator of problematic verification plans; $\overline{r_X}$ was shown to have a relatively higher correlation compared to the indices of modulation, although significance of the difference could not be determined given the small sample size. While both $\overline{r_X}$ and average leaf gap were both related to aperture area, the AP-ratio also considered the exposed MLC leaf edges which had also contributed to the fluence modulation. As the ratio of area to perimeter decreased, a greater proportion of the field was exposed to MLC leaf edges. For this reason, the AP-ratio may be an important consideration in the planning and verification of other treatment modalities, such as RapidArc. The MLC apertures of a RapidArc plan are known to be highly irregular, and for which the simplistic average leaf separation used in describing sliding window IMRT fields may be a less meaningful descriptor of plan complexity.

The calculation of each quantity associated with fluence modulation required averaging complicated properties of each plan, and resulted in a great loss in detailed information. Figure 5.10 shows that a single plan can intrinsically have a high level of variability in aperture geometry, of which most of the information was lost in calculating the AP-ratio. Similarly, mean values of the modulation index neglected much of the plan complexity revealed by the calculation. As shown in Figure 5.7, the relative modulation indices of each field was dependent on the value of $F$ that was used in the calculation of MI. Further development in using fluence related quanti-

ties requires that the parameters of the calculation be optimized. While attributing single-valued, averaged quantities to the complex fluences of an IMRT plan may, in principle, result in a loss of information, meaningful quantities were preserved by this work. These methods led to highly correlated relationships relevant to the IMRT verification process at VIC. Ultimately, the means of quantifying fluence modulation should be specific to the processes under evaluation.

# Chapter 6

# Conclusions and Future Work

All verification failures were shown to be resolved by ensuring the integrity of related instrumentation and implementing the most accurate available methods of dose calculation. EPID malfunction was considered to contribute largely to the production of failures. When repaired, variability of the dose reconstruction measurements were shown to be insignificant to the verification process. Ion chambers were decidedly limited in describing the complicated nature of volumetric discrepancies and were subject to large positioning uncertainties. In any case, both the calculated and EPIDose reconstructed dose distributions agreed reasonably well with the ion chamber measurements. Deficiencies in the PBC and/or the LMC (Eclipse version 8.1.18) were shown to contribute to failures and this was attributable (at least in part) to fluence modulation. The clinical implementation of an advanced dose calculation algorithm (AAA) was shown to completely resolve these types of failures. In addition, the results of EPIDose dose reconstruction were consistent with Monte Carlo dose calculations to within clinically acceptable differences.

These results were derived from a relatively small sample of IMRT plans verified at VIC –at most 21 of more than 300– and therefore may not have been completely representative of clinical verification in practice. A significant increase in the sample size would have required many more verification measurements and was not consid-

ered feasible within the provided time frame of the experiment. Additionally, the natural restrictions of working in a clinical environment prevented more in depth analysis of deficiencies in older versions of the LMC and PBC. Future work may include optimizing the methods of quantifying fluence modulation. The techniques and fluence related software that have been developed may also be adapted to other modalities of external beam radiaton therapy susceptible to problematic levels of fluence complexity (eg. RapidArc). The verification process may also benefit from the implementation of some form of statistical process control. In this way, users could be alerted to statistically significant fluctuations and time dependent trends in verification outcome, allowing for the rapid identification and removal of systematic deficiencies in the process.

# Bibliography

[1] Canadian Cancer Society's Steering Committee. Canadian Cancer Statistics 2010. Toronto: Canadian Cancer Society, 2010.

[2] A Van Der Kogel and M Joiner. *Basic Clinical Radiobiology*. Hodder Arnold, London, England, fourth edition, 2009.

[3] E J Hall and A J Giaccia. *Radiobiology for the Radiologist*. Lippincott Williams and Wilkins, Philadelphia, PA, fifth edition, 2000.

[4] B Emami, J Lyman, A Brown, L Cola, M Goiten, J E Munzenrider, B Shank, L J Solin, and M Wesson. Tolerance of normal tissue to therapeutic irradiation. *Int. J. Radiat. Oncol. Biol. Phys.*, 21(1):109—-122, 1991.

[5] F M Khan. *The Physics of Radiation Therapy*. Lippincott Wiliams and Wilkins, Philadelphia, Pensylvania, third edition, 2003.

[6] A Smith. Vision 20/ 20: Proton therapy. *Med. Phys.*, 36(2):556–568, 2009.

[7] D Schulz-Ertner and H Tsujil. Particle radiation therapy using proton and heavier ion beams. *J. Clin. Onc.*, 25(8):953–964, 2007.

[8] F H Attix. *Introduction to Radiological Physics*. John Wiley and Sons, Toronto, Ontario, 1986.

[9] J Van Dyk, editor. *The Modern Technology of Radiation Therapy*. Medical Physics Publishing, Madison, Wisconson, 2005.

[10] IMRT Colaborative Working Group. Intensity Modulated Radiotherapy: Current status and issues of interest. *Int. J. Rad. Onc. Biol. Phys.*, 51(4):880 –914, 2001.

[11] M Oliver, W Ansbacher, and Beckham W A. Comparing planning time, delivery time and plan complexity for IMRT, RapidArc and tomotherapy. *J. Applied Clin. Med. Phys.*, 10(4), 2009.

[12] T Bortfeld. IMRT : a review and preview. *Phys. Med. Biol.*, 51:R363—-R379, 2006.

[13] S Webb. The physical basis of IMRT and inverse planning. *British Journal of Radiology*, 76:678–689, October 2003.

[14] G Ezzel, J Galvin, D Low, J Palta, I Rosen, M Sharp, P Xia, Y Xiao, L Xing, and C Yu. Guidance document on delivery, treatment planning, and clinical implementation of IMRT: Report of the IMRT subcommittee of the AAPM radiation therapy committee. *Med. Phys.*, 30(8):2089—-2116, 2003.

[15] T LoSasso, C S Chui, and C C Ling. Physical and dosimetric aspects of a multileaf collimation system used in the dynamic mode for implementing intensity modulated radiotherapy. *Med. Phys.*, 25(10):1919—-1927, 1998.

[16] T Pawlicki, S Yoo, L E Court, S K Mcmillan, Roger K Rice, J Donald Russell, John M Pacyniak, Milton K Woo, Parminder S Basran, Jason Shoales, and Arthur L Boyer. Moving from IMRT QA measurements toward independent computer calculations using control charts. *Medical Physics*, 89:330–337, 2008.

[17] W Ansbacher. Three-dimensional portal image-based dose reconstruction in a virtual phantom for rapid evaluation of IMRT plans. *Med. Phys.*, 33(9):3369–3382, 2006.

[18] Jun Deng, Todd Pawlicki, Yan Chen, Jinsheng Li, Steve B Jiang, and C M Ma. The MLC tongue-and-groove effect on IMRT dose distributions. *Phys. Med. Biol.*, 46(4):1039–60, April 2001.

[19] I Chauvet, A Petitfils, C Lehobey, J Y Kristner, Y Brunet, R Lembrez, G Gaboriaud, A Mazal, S Zefkili, and J C Rosenwald. The sliding slit test for dynamic IMRT: a useful tool for adjustment of MLC related parameters. *Phys. Med. Biol.*, 50(4):563–580, February 2005.

[20] M Essers, M de Langen, M L Dirkx, and B J Heijmen. Commissioning of a commercially available system for intensity-modulated radiotherapy dose delivery with dynamic multileaf collimation. *Radiotherapy and oncology : journal of the European Society for Therapeutic Radiology and Oncology*, 60(2):215–24, August 2001.

[21] E Wasbøand H Valen. Dosimetric discrepancies caused by differing MLC parameters for dynamic IMRT. *Phys. Med. Biol.*, 53(2):405–15, January 2008.

[22] P Storchi and E Woudstra. Calculation models for determining the absorbed dose in water phantoms in off-axis planes of rectangular fields of open and wedged photon beams. *Phys. Med. Biol.*, 40:511–527, 1995.

[23] P Storchi and E Woudstra. Calculation of the absorbed dose distribution due to irregularly shaped photon beams using pencil beam kernels derived from basic beam data. *Phys. Med. Biol.*, 41:637–656, 1996.

[24] P Storchi, L Van Battum, and E Woudstra. Calculation of a pencil beam kernel from measured photon beam data. *Phys. Med. Biol.*, 44:2917—-2928, 1999.

[25] A Van Esch, L Tillikainen, J Pyykkonen, M Tenhunen, H Helminen, S Siljamäki, J Alakuijala, M Paiusco, M Lori, and Huyskens D P. Testing of the analytical

anisotropic algorithm for photon dose calculation. *Med. Phys.*, 33(11):4130—-4148, 2006.

[26] J Sievinen, W Ulmer, and W Kaissl. AAA Photon Dose Calculation Model in Eclipse , Varian Medical Systems, Helsinki, 2005.

[27] W Ulmer, J Pyyry, and W Kaissl. A 3D photon superposition/convolution algorithm and its foundation on results of Monte Carlo calculations. *Phys. Med. Biol.*, 50(8):1767–1790, April 2005.

[28] D E Raeside. Monte Carlo principles and applications. *Phys. Med. Biol.*, 21(2):181–197, March 1976.

[29] P Andreo. Monte Carlo techniques in medical radiation physics. *Phys. Med. Biol.*, 36(7):861–920, July 1991.

[30] D W O Rogers. Monte Carlo Techniques in Radiotherapy. *Med. Phys.*, 58(2):63–70, 2002.

[31] A F Bielajew, H Hirayama, W R Nelson, and D W O Rogers. History, overview and recent improvements of EGS4, National Research Council of Canada Report PIRS-0436, 1994.

[32] I Kawrakow and D W O Rogers. The EGSnrc Code System: Monte Carlo simulation of electron and photon transport, National Research Council of Canada, Ottawa, 2000.

[33] J Siebers, P J Keall, J Kim, and R Mohan. A method for photon beam Monte Carlo multileaf collimator particle transport. *Phys. Med. Biol.*, 47:3225–3249, 2002.

[34] B E Nelms and J Simon. A survey on planar IMRT QA analysis. *J. Applied Clinical Medical Physics*, 8(3):2448–2462, January 2007.

[35] H E Johns and J R Cunningham. *The Physics of Radiology*. Charles C Thomas, Springfield, Illinois, fourth edition, 1983.

[36] M Bucciolini, F B Buonamici, and M Casati. Verification of IMRT fields by film dosimetry. *Med. Phys.*, 31:161–168, 2003.

[37] P B Greer and C C Popescu. Dosimetric properties of an amorphous silicon electronic portal imaging device for verification of dynamic intensity modulated radiation therapy. *Med. Phys.*, 30:1618–1627, 2003.

[38] P Munro and D Bouius. X-ray quantum limited portal imaging using amorphous silicon flat-panel arrays. *Med. Phys.*, 25:830–840, 1998.

[39] A Van Esch, T Depuydt, and D Huyskens. The use of an aSi-based EPID for routine absolute dosimetric pre-treatment verification of dynamic IMRT fields. *J. Euro. Soc. for Therapeutic Radiology and Oncology*, 71(2):223–34, May 2004.

[40] P B Greer. Correction of pixel sensitivity variation and off-axis response for amorphous silicon EPID dosimetry. *Med. Phys.*, 32(12):3558–3568, 2005.

[41] G Nicolini, A Fogliata, E Vanetti, A Clivio, and L Cozzi. GLAaS: An absolute dose calibration algorithm for an amorphous silicon portal imager. Applications to IMRT verifications. *Medical Physics*, 33(8):2839–2851, 2006.

[42] A Bakai, M Alber, and F Nusslin. A revision of the $\gamma$ -evaluation concept for the comparison of dose distributions. *Phys. Med. Biol.*, 48:3543–3553, 2003.

[43] R Mohan, M Arnfield, S Tong, Q Wu, and J Siebers. The impact of fluctuations in intensity patterns on the number of monitor units and the quality and accuracy of intensity modulated radiotherapy. *Med. Phys.*, 27(6):1226–1237, June 2000.

[44] Q Hou, C Zhang, Z Wu, and Y Chen. A method to improve spatial resolution and smoothness of intensity profiles in IMRT treatment planning. *Medical Physics*, 31(6):1339–1347, 2004.

[45] M Broderick, M Leech, and M Coffey. Direct aperture optimization as a means of reducing the complexity of intensity modulated radiation therapy plans. *Radiation Oncology*, 4:8–14, 2007.

[46] M Matuszak, E Larsen, K Jee, D Mcshan, and B Fraass. Adaptive diffusion smoothing: A diffusion-based method to reduce IMRT field complexity. *Med. Phys.*, 35(4):1532–1546, 2008.

[47] A McNiven, M Sharpe, and T Purdie. A new metric for assessing IMRT modulation complexity and plan deliverability. *Med. Phys.*, 37(2):505–515, 2010.

[48] S Webb. Use of a quantitative index of beam modulation to characterize dose conformality: illustration by a comparison of full beamlet IMRT, few-segment IMRT (fsIMRT) and conformal unmodulated radiotherapy. *Phys. Med. Biol.*, 48:2051–2062, 2003.

[49] G Nicolini, A Fogliata, E Vanetti, A Clivio, F Ammazzalorso, and L Cozzi. What is an acceptably smoothed fluence? Dosimetric and delivery considerations for dynamic sliding window IMRT. *Radiation Oncology*, 2:42–54, 2007.

[50] BEAM. OMEGA-BEAM Workshop: BEAM Manual, National Research Council of Canada, Ottawa, 1997.

[51] J R Taylor. *An Introduction to Error Analysis: the study of uncertainties in physical measurement*. University Science Books, Sausalito, CA, 1982.